PHOTONIC INTEGRATED CIRCUIT COMPONENTS WITH AMORPHOUS STRUCTURES

A THESIS SUBMITTED TO
THE GRADUATE SCHOOL OF NATURAL AND APPLIED SCIENCES
OF
MIDDLE EAST TECHNICAL UNIVERSITY

BY

MURAT CAN SARIHAN

IN PARTIAL FULFILLMENT OF THE REQUIREMENTS
FOR
THE DEGREE OF MASTER OF SCIENCE
IN
ELECTRICAL AND ELECTRONICS ENGINEERING

JULY 2018

Approval of the thesis:

PHOTONIC INTEGRATED CIRCUIT COMPONENTS WITH AMORPHOUS STRUCTURES

submitted by **MURAT CAN SARIHAN** in partial fulfillment of the requirements for the degree of **Master of Science in Electrical and Electronics Engineering Department, Middle East Technical University** by,

Prof. Dr. Halil Kalıpçılar _____
Dean, Graduate School of **Natural and Applied Sciences**

Prof. Dr. Tolga Çiloğlu _____
Head of Department, **Electrical and Electronics Engineering**

Assist. Prof. Dr. Serdar Kocaman _____
Supervisor, **Electrical and Electronics Engineering, METU**

Examining Committee Members:

Prof. Dr. Özlem Aydın Çivi
Electrical and Electronics Engineering, METU _____

Assist. Prof. Dr. Serdar Kocaman
Electrical and Electronics Engineering, METU _____

Assoc. Prof. Dr. Özgür Ergül
Electrical and Electronics Engineering, METU _____

Assoc. Prof. Dr. İsa Navruz
Electrical and Electronics Engineering, Ankara University _____

Prof. Dr. Barış Akaoğlu
Physics Engineering, Ankara University _____

Date: _____

I hereby declare that all information in this document has been obtained and presented in accordance with academic rules and ethical conduct. I also declare that, as required by these rules and conduct, I have fully cited and referenced all material and results that are not original to this work.

Name, Last Name: MURAT CAN SARIHAN

Signature :

ABSTRACT

PHOTONIC INTEGRATED CIRCUIT COMPONENTS WITH AMORPHOUS STRUCTURES

Sarıhan, Murat Can
M.S., Department of Electrical and Electronics Engineering
Supervisor : Assist. Prof. Dr. Serdar Kocaman

July 2018, 71 pages

In this thesis work, amorphous photonic materials, which are an alternative to photonic crystals and offering flexibility and comparable performance, are designed for photonic integrated circuits and analyzed. A design guideline is presented for the first time with experimental verification in telecommunication wavelengths. Amorphous photonic materials are artificially designed materials that possessing random refractive index distributions and has photonic band gaps due to the inherent short-range order. For the amorphous photonic materials, a Monte Carlo method is proposed which is taking natural crystalline-amorphous semiconductor transitions as an example and the affecting design parameters are analyzed. The generated amorphous structures are analyzed numerically and experimentally for verification. Furthermore, the factors affecting band gap is scrutinized. The band gap asymmetry which is one of the basic properties of amorphous photonic materials are explained theoretically, with the help of electronic amorphous semiconductors.

Keywords: Photonic crystals, Amorphous materials, Photonic integrated circuits

ÖZ

AMORF YAPILAR İLE FOTONİK ENTEGRE DEVRE ELEMANLARI

Sarıhan, Murat Can
Yüksek Lisans, Elektrik ve Elektronik Mühendisliği Bölümü
Tez Yöneticisi : Dr. Öğr. Ü. Serdar Kocaman

Temmuz 2018 , 71 sayfa

Bu tez çalışmasında fotonik tümleşik devreler için fotonik kristal yapılara alternatif, esneklik ve yeterli performans sağlayan amorf fotonik materyaller tasarlanmış ve incelenmiştir. İlk defa, telekomünikasyon dalgaboylarında bir tasarım yol haritası deneysel sağlamaları ile birlikte sunulmuştur. Amorf fotonik malzemeler yapay tasarımlı rastgele kırıcılık indisi dağılımlarına sahip materyaller olup, bünyelerinde barındırdıkları kısa menzilli duzenden dolayı fotonik bant aralıklarına sahiplerdir. Amorf fotonik malzemeler için doğal kristal-amorf dönüşümlerini örnek alan bir Monte Carlo yöntemi tanıtılmış, tasarım parametreleri incelenmiştir. Üretilen amorf yapılar sayısal ve deneysel olarak incelenmiş ve teyit edilmiştir. Ayrıca, bant aralığını etkileyen faktörler incelenmiştir. Amorf fotonik malzemelerin temel özelliklerinden olan bant aralığı asimetrisi, elektronik amorf yarıiletkenlerden yararlanarak teorik olarak açıklanmıştır.

Anahtar Kelimeler: Fotonik kristaller, Amorf malzemeler, Fotonik entegre devreler

To my beloved ones...

ACKNOWLEDGMENTS

The author wishes to express his deepest gratitude to his supervisor Assist. Prof. Serdar Kocaman, for introducing him to fascinating field of photonics, his valuable contributions on the conception of this thesis work and his guidance in the author's academic and career development.

The author would also like to thank Alperen Gövdeli for his help and contributions on the experimental verification of the study.

The author would like to gratefully acknowledge the valuable discussions and contributions of Prof. Chee Wei Wong from University of California, Los Angeles and Prof. Şakir Erkoç from Middle East Technical University. Furthermore, the author expresses his gratitude to Assoc. Prof. İsa Navruz for lending an optical spectrum analyzer that provides the most accurate results for this thesis study.

The author wishes to thank gladly for the supports and motivations to his family Aysen Sarıhan and Hasan Onurcan Sarıhan, his beloved friends and Selin Kızılgün, who have never left alone during the preparation of this thesis.

The author would like to recognize the help of his friends Dilge Kanoğlu, Alper Kılıç, Alican Özkan, Uğur Berkay Saraç and Seyit Yiğit Sızlayan; for proofreading this work and their most valuable recommendations.

During the procession of this study, the author acknowledges the financial support of TUBITAK BIDEB 2210-A 2016-1 Graduate Scholarship Program to him.

TABLE OF CONTENTS

LIST OF TABLES

TABLES

LIST OF FIGURES

FIGURES

LIST OF ABBREVIATIONS

B	Magnetic flux density
E	Electric field intensity
D	Electric displacement field
H	Magnetic field intensity
ε_0	Electric permittivity of free space
ε_r	Dielectric constant of medium
TE	Transverse-electric (polarization)
TM	Transverse-magnetic (polarization)
2-D	Two-dimensional
3-D	Three-dimensional
EM	Electromagnetic
J	Current density
ρ	Charge density
μ_0	Magnetic permeability of free space
μ_r	Magnetic constant of medium
ω	Frequency
c	Speed of light
H	Hamiltonian
PBG	Photonic band gap
LDoS	Local density of states
DoS	Density of states
FDTD	Finite-difference time-domain method
PML	Perfectly matched layer
PBC	Periodic boundary condition

PEC	Perfect electric conductor
FFT	Fast Fourier transform
IBZ	Irreducible Brillouin zone
PEF	Potential energy functions
g(R)	Radial distribution function
SOI	Silicon on insulator
PMMA	Polymethyl methacrylate
BOE	Buffered oxide etchant
SEM	Scanning electron microscopy
ASE	Amplified spontaneous emission
ICP	Inductively coupled plasma
RIE	Reactive ion etching

CHAPTER 1

INTRODUCTION

1.1 Overview

Photonic crystals are artificially designed periodic structures that can control the propagation of light in a way like semiconductor crystals affecting electrons in electronic devices, through band gap. Thus, they become prominent candidates as the building blocks of the emerging photonic integrated circuit technologies for optical computing and communications. With the invention of the first photonic crystal having a complete bandgap [1], tremendous efforts of research are put to meet the demands of our age in terms of computing power and data throughput [2, 3, 4, 5].

The core of photonic crystals lies in their periodicity. In order to utilize band gaps to control light propagation, the satisfaction of Bloch's theorem is essential [2]. Formation of photonic bands that ensure complete band gaps are disturbed when Bloch's theorem is violated through imperfections in the periodicity of structural refractive index variations. Nevertheless, it is very hard to preserve the periodic order through practical applications, especially during their fabrication. Due to this fact, effect of disorder on photonic crystal operations is being addressed since a long time [6, 7, 8, 9, 10]. Another issue is, for some applications, the creation of defects inside photonic crystal lattice is essential, especially for some cavity and waveguide applications. To achieve that without disturbing photonic crystal operation, it is mandatory to follow the periodicity axes inside the structure. Thus, flexible designs are not possible.

To overcome these limitations, considering disorder as an advantage instead of an imperfectness which is required to be eliminated is an interesting idea. Amorphous photonic materials are originated from this concept. Like the relationship between

crystalline and amorphous semiconductors, amorphous photonic materials are still able to control light propagation in the absence of periodicity, which is counterintuitive to Bloch's theorem. This ability is due to the inherent short range order in the refractive index variations among the structure even in the absence of long-range periodicity.

1.2 Previous Studies on Amorphous Photonic Materials

The study of disorder and randomness on amorphous photonic materials has started around the same time that the photonic crystals have postulated by Yablonovitch [1]. First, Sajeev John has theorized the existence of a frequency regime for EM waves to undergo Anderson localization in three dimensions which causes the formation of a mobility edge in the 1980's. Later, he proved the existence of a band gap consisting localized states which is marked by two mobility edges separating higher and lower frequency extended states in artificially designed disordered superlattices [11, 12]. These studies have been validated for the random two-component medium with a dielectric constant contrast by demonstrating localization of classical waves in medium [13]. In the 90's, the research on periodic dielectric structures like photonic crystals intensified. Experimental verification of amorphous photonic materials has only been done in 2001 by Jin [14]. In this study, amorphous materials is designed by randomly rotating square unit cells of a 2-D photonic crystal to demonstrate a S-polarized band gap at microwave regime. Later, the first guidelines for flexible waveguides on photonic integrated circuit applications are shown by Miyazaki et.al. [15] and Kwan et.al. [6]. In these studies, the most efficient waveguide design are shown by placing one line of equally distanced scatterers to each side of opened waveguide defect. It is followed by the demonstration of a photonic amorphous diamond structure with a complete 3-D gap [3]. For amorphous structures with 2-D random index variations, different design methods are proposed. Among them, Florescu et. al. [16] has proposed an optimization algorithm that produces a pseudo-random network which is based on hyperuniformity concept . In another study, the transition of photonic material structure from crystalline to amorphous is analyzed by following polycrystalline formations as an intermediary [17]. Furthermore, natural methods based on

mimicking amorphous semiconductor glass formation utilizing molecular simulation methods are used. Rechtsman et. al. conducted a Monte Carlo simulation by considering 2-D rod scatterers as particles in liquid-like structure and evolved the positions of scatterers inside the medium via Metropolis method. With this way, existence of a band gap around visible optical regime is demonstrated [18]. With a similar technique, Kocaman et.al. [19] put some efforts to design an amorphous structure that has a band gap at near-infrared around telecommunication frequencies to be directly used in optical telecommunication circuits.

This thesis study aims to demonstrate first time, an amorphous photonic slab with air hole scatterers operating at near-infrared telecommunications regime in detail, with experimental verifications. A design guideline for such structures is also proposed first time by examining variables affecting amorphous configuration generation and the band gap properties. The differences between band-gap characteristics of photonic crystals and amorphous counterparts are identified and explained by establishing an analogy with amorphous glassy semiconductors. With this way, the thesis offers a comprehensive guideline for the utilization of such materials in growing number of photonic integrated circuit applications. The study is submitted to be presented at high-impact conferences and a manuscript is prepared for peer-review in a high-reputation journal.

1.3 Thesis Organization and Research Focus

The focus of this thesis work is presenting amorphous photonic materials for flexible photonic integrated circuit applications. For this purpose, a design guideline will be presented and properties of the photonic band gap of the material will be analyzed in every aspect. The existence of such materials is demonstrated experimentally through conventional Si fabrication and analysis methods. The distinctive properties of the band gap are explained in analogy with the crystalline-amorphous semiconductor differences.

In the first chapter, the problem and previous studies on the topic are briefly presented. In the second chapter, the theoretical foundations and governing functions of amor-

phous materials are explained with the addition of general photonic crystal theory. The third chapter presents the main numerical analysis methods for photonic material design, FDTD and eigenmode solvers. In the fourth chapter, the wave propagation is analyzed inside amorphous electronic and photonic materials theoretically and common analogies are drawn. In the fifth chapter, the generation of random refractive index distributions for amorphous photonic materials via Monte Carlo simulations is explained and affecting design parameters are analyzed. In the sixth chapter, numerical analysis results are presented for amorphous photonic materials and the dominant gap characteristics are explained in analogy with electronic semiconductor materials In the seventh chapter, the device fabrication, and experimental verification steps are explained with measurement method.

CHAPTER 2

THEORY OF PHOTONIC CRYSTALS

2.1 Functions Governing Photonic Materials

For macroscopic systems, scattering of electromagnetic fields in a dielectric medium is governed by the four equations of Maxwell [20], which are given at (2.1).

$$\begin{aligned} \vec{\nabla} \cdot \vec{B} &= 0 \\ \vec{\nabla} \cdot \vec{D} &= \rho \\ \vec{\nabla} \times \vec{E} &= -\frac{\partial \vec{B}}{\partial t} \\ \vec{\nabla} \times \vec{H} &= \vec{J} + \frac{\partial \vec{E}}{\partial t} \end{aligned} \tag{2.1}$$

In this case, the aforementioned medium is a mixed dielectric, which has spatially varying dielectric constant. In order to solve the wave behavior in the medium, a unified equation to solve fields is needed. To achieve that, the following assumptions are made: First, the effective permittivity of the medium is linear and isotropic; i.e., does not change with field intensity and it is a scalar identity. Second, unless specified, there is not any source of light present in the medium. In this case, charge and current densities $\rho = 0$ and $J = 0$. Third, the medium is assumed to be non-magnetic; that is, $\mu_r = 1$. Finally, if it is considered that the medium is non-dispersive and transparent for the solution of the problem, a positive-real and frequency-independent dielectric constant is obtained [2]. This is useful to model the eigenvalue problem determining the propagating electromagnetic modes over the system.

As a result of these assumptions, the Maxwell equations in (2.1) become:

$$\begin{aligned} \vec{\nabla} \cdot \vec{B} &= 0 \\ \vec{\nabla} \cdot \vec{D} &= 0 \\ \vec{\nabla} \times \vec{E} &= -\mu_0 \frac{\partial \vec{H}}{\partial t} \\ \vec{\nabla} \times \vec{H} &= \varepsilon_0 \varepsilon_r(r) \frac{\partial \vec{E}}{\partial t} \end{aligned} \tag{2.2}$$

Based on these assumptions, since the Maxwell's equations are linear; separation of spatial and temporal variables can be achieved to solve the system. Moreover, the solution can be expressed as the superposition of harmonic solutions (modes) through Fourier analysis for each frequency component. The harmonic expression of fields are provided as:

$$H(r,t) = H(r)e^{-j\omega t} \tag{2.3}$$

$$E(r,t) = E(r)e^{-j\omega t} \tag{2.4}$$

By inserting the solutions (2.3) and (2.4) into the equations of (2.2), in the absence of external sources, the time-harmonic equivalents of Maxwell's equation are obtained.

$$\vec{\nabla} \cdot \vec{H} = 0 \tag{2.5}$$

$$\vec{\nabla} \cdot (\varepsilon \vec{E}) = 0 \tag{2.6}$$

$$\vec{\nabla} \times \vec{E} = j\omega\mu_0 \vec{H} \tag{2.7}$$

$$\vec{\nabla} \times \vec{H} = -j\omega\varepsilon_0\varepsilon_r(r)\vec{E} \tag{2.8}$$

In order to obtain a complete solution for the eigenproblem, it is needed to combine equations (2.7) and (2.8). Multiplying (2.7) by ε_r^{-1} and taking the curl of it, the two equations could be combined. The resulting equation is the master wave equation for magnetic field.

$$\vec{\nabla} \times (\frac{1}{\varepsilon_r} \vec{\nabla} \times \vec{H}) = (\frac{\omega}{c})^2 \vec{H} \tag{2.9}$$

Analogous of the equation (2.9) for the electric field is:

$$\frac{1}{\varepsilon_r} \vec{\nabla} \times (\vec{\nabla} \times \vec{E}) = (\frac{\omega}{c})^2 \vec{E} \tag{2.10}$$

These two equations are capable of providing every information required to describe behavior of light in the media. Furthermore, an important property of the solutions of

these equations is that there is not any fundamental length scale in contrast with quantum mechanics [2]. All the solutions can be scaled in terms of wavelength, frequency and lattice dimensions. In order to demonstrate, assume that the medium dimensions are scaled such that $\vec{r}' = s\vec{r}$, $\varepsilon_r(\vec{r}) = \varepsilon_r(\vec{r}')$ and $\vec{\nabla}' = \frac{1}{s}\vec{\nabla}$. Applying these conditions to the master wave equation, the following (2.11) is obtained.

$$\vec{\nabla}' \times (\frac{1}{\varepsilon_r(\vec{r}')}\vec{\nabla}' \times \vec{H}(\vec{r}'/s)) = (\frac{\omega}{sc})^2 \vec{H}(\vec{r}'/s) \tag{2.11}$$

It can be deduced from (2.11) that, when the dimensions of the medium is scaled by "s", the field amplitude and eigenfrequency of the modes are scaled by the same amount,"s"; i.e., $\vec{H}'(\vec{r}') = \vec{H}(\vec{r}'/s)$ and $\omega' = \omega/s$.

For the procession of thesis, it will be essential to identify the parallelism between quantum mechanics and electromagnetics. Thus, it could be beneficial to define (2.9) as an operator providing the eigenvalue of the system as a result. This will make the wave equation similar to Schrödinger's equation of quantum mechanics.

$$\hat{\Theta}_H = \vec{\nabla} \times \frac{1}{\varepsilon_r}\vec{\nabla}\times \tag{2.12}$$

$$\hat{\Theta}_E = \frac{1}{\varepsilon_r}\vec{\nabla} \times \vec{\nabla}\times \tag{2.13}$$

Considering the Hamiltonian operator of Schrödinger's equation, $\hat{H} = -\frac{\hbar^2}{2m}\nabla^2 + V(r)$ (V is the potential energy), both equations become similar in terms of form and properties.

$$\hat{\Theta}_{\vec{H}}\vec{H} = (\frac{\omega}{c})^2 \vec{H} \tag{2.14}$$

$$\hat{H}\Psi = E\Psi \tag{2.15}$$

Both equations indicate an eigenvalue problem that determines the energy, E (i.e. frequency, ω for light) level the wave function can exist. In order to summarize the similarities; both operators are linear and Hermitian (except $\hat{\Theta}_E$). The eigensolutions for the corresponding wavefunctions can be shown as linear combinations of harmonic modes. The resultant eigenvalues of Hermitian operators are real and their eigenvectors form a complete and orthogonal set [2]. In quantum mechanics, the wave functions of harmonic modes are complex scalar fields, while in electromagnetics, they are real vector fields with assigned complex exponentials. In quantum mechanics, the spatial energy distribution is concentrated in low potential regions for

lowest eigenstates, while electromagnetic fields are more confined into the regions with high dielectric constant for low-frequency modes [2]. The difference is, the Hamiltonian of quantum mechanics is separable if the potential energy operator $V(r)$ is separable, while it is not possible for classical wave equation for most of the time. Still, the behaviors are same under periodic media for quantum mechanical and electromagnetic cases. As it will be mentioned in chapter four, they are both subjected to Bloch's theorem and can form degenerate states under various wavevectors according to periodicity of the medium [2]. The importance of this relations is that the postulates applied to electronic properties of semiconductors can be mostly carried to the electromagnetic regime for photonic crystal dynamics.

2.2 Structure of Photonic Crystals

The smallest indivisible element of a photonic crystal is unit cell, which contains the irreducible refractive index variation repeated periodically over an infinite space [2]. The crystal structure possesses discrete translational symmetry; that is, refractive index distribution is invariant over distances that are multiples of a fixed length called lattice constant, a. For both electromagnetics and quantum mechanics, symmetries play a big role and provide a convenient intuition about the supported modes of the system. The unit cell is duplicated over the space according to the primitive lattice vectors of the system. The subset of these vectors, $\vec{a_1}, \vec{a_2}, \vec{a_3}$, forms the basis of the crystal. Any unit cell along the lattice can be defined as linear combination of these vectors, e.g. $\vec{R} = n_1\vec{a_1} + n_2\vec{a_2} + n_3\vec{a_3}$. Thus, the refractive index variation over the system can be defined in terms of the unit cell as indicated by (2.16).

$$\varepsilon_r(\vec{r}) = \varepsilon_r(\vec{r} + \vec{R}) \tag{2.16}$$

Since the permittivity of the lattice is periodic, it is logical to analyze the distribution by Fourier transform.

$$\varepsilon_r(\vec{r}) = \int d^3 f(\vec{G}) e^{j\vec{G}\cdot\vec{r}} \tag{2.17}$$

Repeating it for $\varepsilon_r(\vec{r} + \vec{R})$ due to equation (2.16);

$$\varepsilon_r(\vec{r} + \vec{R}) = \int d^3 f(\vec{G}) e^{j\vec{G}\cdot\vec{r}} e^{j\vec{G}\cdot\vec{R}} \tag{2.18}$$

In order to make the equation true, $f(\vec{G}) = f(\vec{G})e^{j\vec{G}\cdot\vec{R}}$ must be satisfied. It is possible when the applied Fourier transform must be zero everywhere, except the values of $\vec{G}$ satisfying $\vec{G}\cdot\vec{R} = 2\pi k, \forall \vec{R}\ and\ k \in N$ [21].

The vectors $\vec{G}$ satisfying the transform form the "reciprocal lattice" of the crystal. In principle the lattice and reciprocal basis vectors of the crystal are convertible vice versa. They are kind of inverses, when the lattice constant of the lattice increases; the reciprocal vectors shrink in reciprocal domain. Similarly, the unit cell of the lattice has an equivalent in reciprocal domain, which is called as the "Brillouin zone" The irreducible element of a reciprocal lattice divided into Brillouin zones is called the first Brillouin zone. The first Brillouin zone possesses all the information about the behavior of an infinite photonic crystal under electromagnetic field. Since the planar photonic crystals slabs is under the scope, the most important Brillouin zone configurations for us are triangular (hexagonal) and square lattices. These configurations are identified with following basis vectors given in Table 2.1.

Table 2.1: The principal symmetry axes (basis) in primitive and reciprocal domain for common 2-D photonic crystal lattice configurations.

		Square Lattice	Hexagonal Lattice
Primitive Vectors:	$\hat{a_1}$	$a\hat{x}$	$a(\hat{x}+\sqrt{3}\hat{y})/2$
	$\hat{a_2}$	$a\hat{y}$	$a(\hat{x}-\sqrt{3}\hat{y})/2$
Reciprocal Vectors:	$\hat{b_1}$	$(\frac{2\pi}{a})\hat{x}$	$(\frac{2\pi}{a})(\hat{x}+\sqrt{3}\hat{y})$
	$\hat{b_2}$	$(\frac{2\pi}{a})\hat{y}$	$(\frac{2\pi}{a})(\hat{x}-\sqrt{3}\hat{y})$

2.3 Bloch's Theorem, Symmetries and Photonic Bands

Due to discrete translational symmetry in primitive and reciprocal lattices, the Hermitian operators $\hat{\Theta}_H$ and $\hat{\Theta}_E$ must be commutative with the translation operator, $\hat{T}_R f(\vec{r}) = f(\vec{r}+\vec{R})$ which is applied along the lattice vectors. The commutativity provides that for the two unit cells, which one of them is the translated version of the other, the eigenfield solution of the wave equation is as follows:

$$\vec{H}(\vec{r}+\vec{R}) = e^{j\vec{k}\cdot\vec{R}}\vec{H}(\vec{r}) \tag{2.19}$$

It can be inferred that, the solution over the primitive domain of the lattice can be expressed with a periodic solution restricted in the unit cell and the translations along the translation vector $\vec{R}$. This theorem is called Bloch's theorem, and its eigensolutions are called as Bloch modes [22, 23]. The eigensolutions can be expressed as linear combinations of the Bloch modes. In order to do that, the wave equation is solved over the first Brillouin zone in the reciprocal domain via Fourier transform.

Let the $\vec{k}$ be the wave-vector corresponding to eigensolution within the first Brillouin zone, then;

$$\vec{H}(\vec{r}) = \sum_{G} H_G e^{j(\vec{k}+\vec{G})\cdot\vec{R}} \tag{2.20}$$

Bloch's theorem states that, the modes identified by $\vec{k}$ and the iterations over the reciprocal domain $\vec{k}+\vec{G}$ are the equivalent modes. These modes can be interpreted as the superpositions of plane waves characterized over the reciprocal domain. Let the periodic part of the mode is identified as $\vec{u}_k(r)$ and insert the Bloch mode to find a solution.

$$\hat{\Theta}_{\vec{H}}\vec{H} = (\frac{\omega(\vec{k})}{c})^2\vec{H} \tag{2.21}$$

$$\vec{\nabla}\times\frac{1}{\varepsilon_r}\vec{\nabla}\times\vec{u}_k(r)e^{j\vec{k}\cdot\vec{r}} = (\frac{\omega(\vec{k})}{c})^2 u_k(r)e^{j\vec{k}\cdot\vec{r}} \tag{2.22}$$

$$(j\vec{k}+\vec{\nabla})\times\frac{1}{\varepsilon_r}(j\vec{k}+\vec{\nabla})\times\vec{u}_k(r) = (\frac{\omega(\vec{k})}{c})^2\vec{u}_k(r) \tag{2.23}$$

The left hand side of the last equation forms a new operator depending on the wave-vector $\vec{k}$. Due to the periodic boundary conditions imposed on the field function $\vec{u}_k(r)$, it can be indicated that the eigenvalue problem is now restricted to the unit cell of the photonic crystal lattice [21]. As a result of the restriction, for each $\vec{k}$, the frequencies of the modes that are supported by the lattice are discretely distributed. Moreover, the k values over the lattice are continuous. Thus, the frequency of each mode should vary with the $\vec{k}$ vector. Based on these information, the dispersion relation $\omega(\vec{k})$ indicating the supported modes for a photonic crystal lattice is comprised by discretely spaced bands continuously varying with the $\vec{k}$ vector. The overall structure is named as the band structure of the photonic crystal and every discrete band is indicated by the band index, n.

In addition to the discrete translational symmetry, the photonic crystal lattices are

invariant under rotational symmetry and the mirror symmetry. The rotational symmetry allows folding the first Brillouin zone itself into its irreducible zone. Solving the eigenvalue equation over the wave-vectors at the edge of the irreducible Brillouin zone provides the complete solution of the whole lattice. Furthermore, with the help of mirror symmetry, the modes can be interpreted as the superposition of polarizations TE and TM [2].

While solving photonic band structure for a given configuration, the symmetries play a huge role to restrict the problem into a very compact, irreducible zone. The discrete translational symmetry has examined before, and enabled the restriction to the Brillouin zone. There are other symmetries in a photonic crystal lattice to fold the Brillouin zone. First symmetry type is rotational symmetry that indicates the invariance of the mode under rotation [2, 21]. The rotation operator is given as $\hat{O}_R$.

$$\hat{O}_R \cdot f(\vec{r}) = Rf(R^{-1}\vec{r}) \tag{2.24}$$

and R indicates the amount of rotation. The operator should be commutative in order to make the mode invariant.Thus,the following arrangements can made.

$$\hat{\Theta}(\hat{O}_R\vec{H}_k n) = \hat{O}_R(\hat{\Theta}\vec{H}_k n) = (\omega_n(\vec{k})/c)^2(\hat{O}_R\vec{H}_k n) \tag{2.25}$$

From the equation above, it can be inferred that applying rotation to a wave vector $\vec{k}$, do not change the eigensolutions, i.e., $\omega_n(R\vec{k}) = \omega_n(\vec{k})$.

Another symmetry is time-reversal symmetry. Since the Maxwellian wave equation is Hermitian, the resultant eigenvalues are real for lossless media. Thus, the complex conjugate of the field H^*_{kn} can be identified by the wave-vector $-\vec{k}$. The result is,

$$\omega_n(\vec{k}) = \omega_n(-\vec{k}) \tag{2.26}$$

The last symmetry form that is affecting the eigenvalue problem is the mirror symmetry. It allows the separation of solution into its polarization components of the field. By defining a mirror reflection operator $\hat{O}_M$ assumed as commutative with Maxwellian operator, $\hat{\Theta}$, the following can be shown.

$$\hat{O}_M\vec{H}_k(\vec{r}) = M\vec{H}(M\vec{r}) = e^{j\phi}\vec{H}_{M\vec{r}} \tag{2.27}$$

Due to the condition above, the eigenvalue equation must satisfy,

$$\hat{O}_M \vec{H}_k(\vec{r}) = \pm \vec{H}_k(\vec{r}) = M\vec{H}_{M\vec{r}} \tag{2.28}$$

The conditions also apply to electric fields, and indicates that the electric and magnetic fields should be even or odd in order to satisfy the operation. However, this separation operation is applicable only if $M\vec{k} = \vec{k}$ to obey $[\hat{\Theta}, \hat{O}_M] = 0$ commutativity check. In particular, it is possible to satisfy these conditions for a two-dimensional photonic crystal lattice. Such crystals have discrete translational symmetry throughout a plane xy; however, uniform along the perpendicular axis z. It enables that the modes of the lattice can be separated into two polarizations due to symmetry in z-axis. The first polarization is transverse-electric (TE),which the electric field propagates along the xy plane with components (E_x, E_y, H_z) and the second is transverse-magnetic (TM) with a confined magnetic field along xy plane with components (H_x, H_y, E_z). This polarization scheme can be preserved for a photonic crystal slab which has finite thickness along z-axis, and identified as TM- or TE-like.

2.3.1 Properties of Photonic Band Diagrams

Band diagram is calculated by solving (2.23) over the $\vec{k}$ points encompassing the irreducible Brillouin zone edge. This edge is passing through the symmetry axes of the lattice and contains the extrema information for all bands. These symmetry axes are expressed by $\vec{k}$ vectors and named according to the lattice type. For example, hexagonal lattices have three symmetry axes named as Γ, M and K. For hexagonal and square lattices, the symmetry axes are shown at Figure 2.1.

The bands are independent of lattice constant, a and frequency values are normalized to satisfy $f \cdot \lambda = 1$ Thus the normalized frequency can be converted to actual wavelength values by dividing a to the frequency.

In the band diagram which is given in Figure 2.2, there are some frequency intervals that has no corresponding allowed state through the $\vec{k}$ over the irreducible Brillouin zone. These intervals are called as photonic band gaps (PBG). It is desired for the photonic crystals to have a complete band gap over all directions and polarizations. 3-D photonic crystals having complete band gaps are demonstrated before [3, 1].

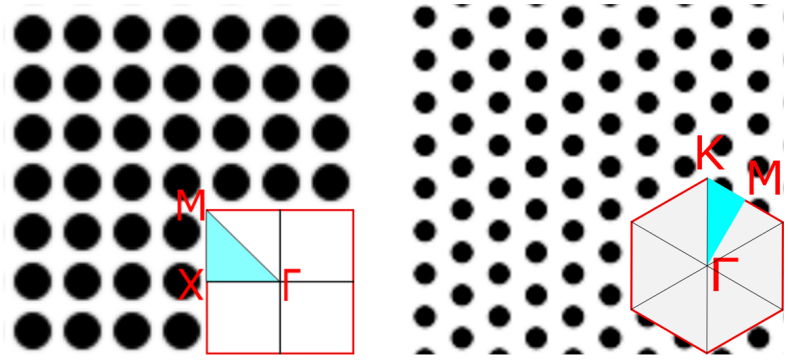

Figure 2.1: The lattice configurations and Brillouin zone with principal symmetry axes for 2-D square and hexagonal lattices are given.

However, such configurations are hard to fabricate. The most common photonic crystal configurations are planar photonic crystal slabs, which combine the properties of 2-D photonic crystals and index guiding along the third dimension.

Index guiding relies on one of the best-known properties of geometrical optics, total internal reflection. Once light is coupled inside the high-dielectric medium, it remains confined for steeper incidence angles. The threshold is named as critical angle and predicted by the Snell's law, $n_{dielectric} * \sin\theta_c = n_{background} * \sin\pi/2$. The Snell's law has two important property that are conservation of frequency (i.e. energy) and momentum, (i.e. wavevector, $\vec{k}$) along the interface. Since there is continuous translational symmetry along the z-axis, the wavevector component along the boundary should be conserved. The dispersion relation between frequency and wavevector is identified as given below and can be decomposed accordingly [2].

$$|k| = \frac{n\omega}{c} = \sqrt{k_{\parallel}^2 + k_{\perp}^2} \tag{2.29}$$

$k_{\parallel}$ must be conserved to be confined inside the medium while $k_{\perp}$ can take arbitrary values. Different combinations of those components create superpositions of plane waves for every possible frequency. However, not all the possible modes are supported by the medium. The limit that defines the supported modes are along the $\omega = ck_{\parallel}$ when $k_{\perp} = 0$. This limit is known as light line and the region of the band structure that possesses unsupported modes, i.e. modes that $\omega > ck_{\parallel}$ is defined as the

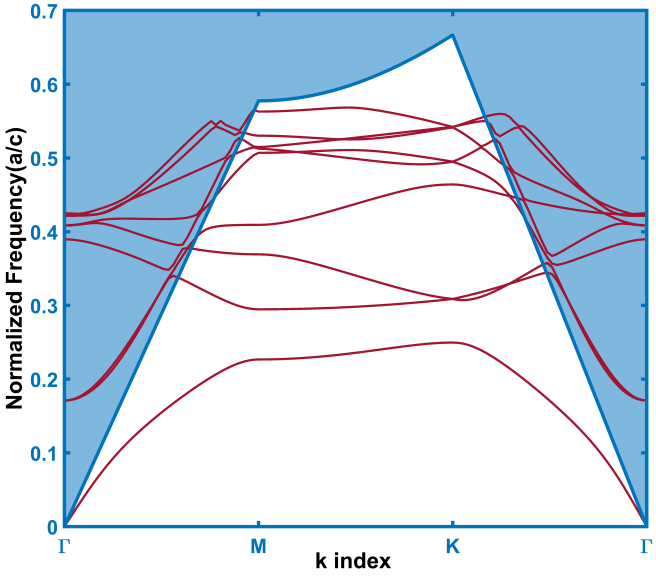

Figure 2.2: A sample TE band diagram of a photonic crystal slab is given. Blue region indicates the light cone. The parts of bands residing in blue region is unsupported because of index guiding.

light cone. The modes that are below the light line have imaginary $k_\perp$ as it can be calculated from (2.29) undergo total internal reflection. This enables that planar slab structures can have pseudo-complete band gaps.

2.3.2 Density of States

Another measure of the photonic crystals is density of states. The density of states indicates the number of allowed modes in the lattice per unit frequency. This measure is very important to understand localization effects of defects, transmission spectra and some nonlinear effects on the lattice such as Purcell effect [24, 25]. The mathematical definition of the DoS is given at equation (2.30) [26].

$$\rho(\omega) = \sum_n \int_{IBZ} d^3k \sigma(\omega - \omega_n(\vec{k})) \tag{2.30}$$

For a periodic lattice, it is possible to compute DoS over the irreducible Brillouin zone. The intervals with zero density along the DoS spectra indicate the photonic band gaps of the lattice. However, in the analyses over real photonic crystals it can

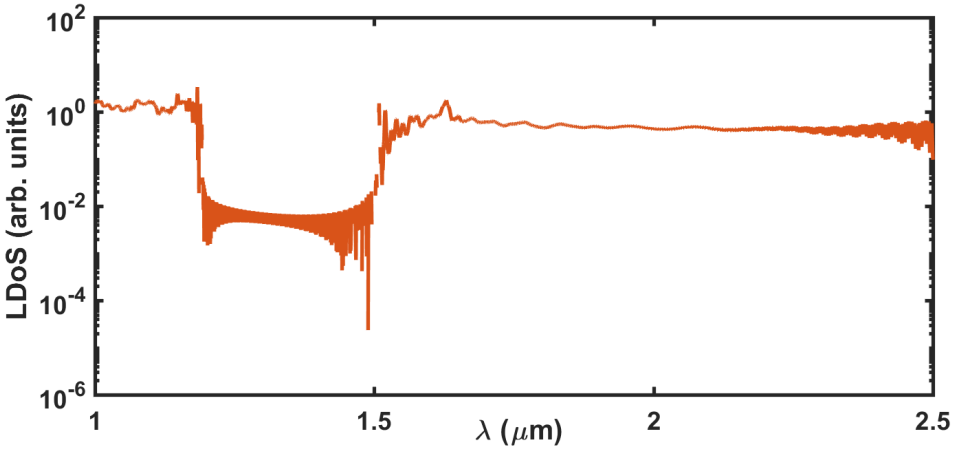

Figure 2.3: The local density of states (LDoS) spectrum of a sample photonic crystal is given as example. The band gap region is easily identifiable. The finite states at gap region is caused by finiteness of simulation region, which is conducted by finite-difference time-domain method.

be observed small, nonzero amount of states due to the finiteness. In the Figure 2.3, these states can be observed. At the boundaries separating band gap and transmission regions, which is called as mobility edge, there are some singularities which is stated before by Van Hove for electronic band gaps [27].

A generalized density of states function is undefinable for disordered and amorphous lattices. For this purpose, local density of states (LDoS) functions are defined to study the transmission properties and localization. It can be measured indirectly from the power radiated by a unit dipole inside the crystal through finite-difference time-domain simulations [24].

$$\rho_l(\vec{x}_0,\omega) = \frac{-2}{\pi}\epsilon(\vec{x}_0)\frac{Re[\hat{E}_l(\vec{x}_0,\omega)\hat{p}(\omega)^*]}{|\hat{p}(\omega)|^2} \tag{2.31}$$

The density of states spectrum can be used to get information about the light transmission, defect and localized modes, resonant enhancements etc. Furthermore, photonic band gap locations can easily be verified through DoS spectrum.

CHAPTER 3

NUMERICAL METHODS FOR PHOTONIC MATERIALS

In this chapter, the common computational methods for photonic crystal analysis are described, which are also frequently used in this study for numerical design, analysis and verification. They are essentially different ways to solve Maxwell's equations over the domain. In this study, the methods that have been used are finite-difference time-domain (FDTD) for transmission and field spectra analyses and plane-wave eigensolvers to compute the photonic band diagrams.

3.1 Finite Difference Time Domain Method (FDTD)

The FDTD method is one of the most effective methods to solve complex devices. It provides direct solutions to the Maxwell equations over a domain with a straightforward method. It is possible to conduct spectral analysis over a large bandwidth since it is a time domain method. The formulation of FDTD method has been done by Yee in 1966 [28]. His algorithm is capable of handling both electric and magnetic fields simultaneously and constructs a geometrical approach to sample over spatial domain. The accuracy of the method is second order and some precautions have been taken in order to increase numerical stability [29]. In order to increase numerical stability, the features of the meshing over the domain should be around $\lambda/20$ and $\lambda/30$.

For a linear, non-dispersive and isotropic material, the Maxwell equations that need to be solved can be written as (3.1) and (3.2). In this case, effect of electrical and magnetic losses (conductivity) is taken into account by σ and σ^*.

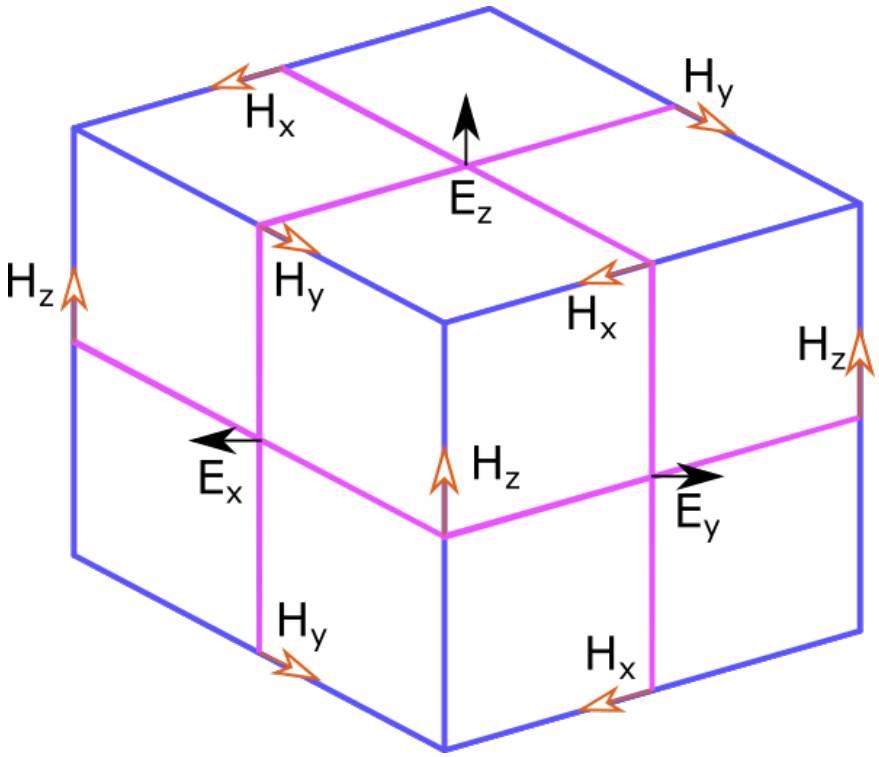

Figure 3.1: The positions of field components of a gridded domain in FDTD according to Yee's algorithm.

$$\frac{\partial \vec{H}}{\partial t} = -1/\mu \nabla \times \vec{E} - 1/\mu\sigma^* \vec{H} \tag{3.1}$$

$$\frac{\partial \vec{E}}{\partial t} = 1/\epsilon \nabla \times \vec{H} - 1/\epsilon\sigma \vec{E} \tag{3.2}$$

These equations can be expanded to six coupled equations for each vectoral component, E_x, E_y, E_z and H_x, H_y, H_z. The system of equations are capable of solving any arbitrary medium in three-dimensions. The Yee's algorithm is offering a way to discretize the equations and solve by approximation in time and spatial domain.

The FDTD algorithm discretizes the fields by placing them over the grid in a way that each E-field component are surrounded by four H-field components, which is shown in Figure 3.1. The partial derivatives are written as finite differences centering the corresponding grid point. The resultant form of the equation is that,

$$\frac{\partial E_y}{\partial z}|_{(i+1/2,j,k)} \approx \frac{E_y(i+1/2,j,k+1/2) - E_y(i+1/2,j,k+1/2)}{\Delta z} \tag{3.3}$$

Similarly, in time domain, center difference method is used to discretize time. With a leapfrogging approach, the fields can be update in two time steps completely. First;

$$\frac{\partial H_x}{\partial t}|_{n\Delta t} \approx \frac{H_x((n+1/2)\Delta t) - H_x((n-1/2)\Delta t)}{\Delta t} \tag{3.4}$$

When the equations (3.3) and (3.4) are placed into (3.1), a discretized form of the Maxwell's equation which can be solved by FDTD algorithm is obtained. The FDTD solves it in two steps: First, $\vec{E}$ is computed using previous value of E and current value of H. Then H is updated by using its previous value and the recently updated value of E. Thus, in two time steps, whole field distribution gets updated. The numerical stability of this operation necessitates a maximum value on time step Δt. For a 3-D simulation domain, the criterion is as follows:

$$\Delta t \leq \frac{1}{c\sqrt{(1/\delta x)^2 + (1/\delta y)^2 + (1/\delta z)^2}} \tag{3.5}$$

For cubic gridding, this criterion becomes $\Delta t \leq \Delta_{x,y,z}/c\sqrt{3}$. In practical applications, in order not to exceed this limitation a constant named as Courant factor is chosen. Courant factor is used to compute a time step according to grid resolution [29].

Another important aspect of FDTD computations is choosing a suitable boundary condition. Since the computational domains must be finite for effectiveness, the medium must be truncated suitably to obtain correct solutions. Such conditions may be reflectors or absorbers. One of the most common and effective boundary conditions is perfectly matched layers (PML) described by Berenger in 1994 [30].

According to PML model, the Maxwell's six curl equations in 3-D is changed with 12 direction dependent equations. This enables that, any plane wave with normal incidence to the domain boundary can pass through the PML layer with no reflection.

Another boundary condition is periodic boundary condition (PBC). It is very suitable to reduce computational domain to the smallest element in infinite periodic lattices. The fields are obtained over the unit cell by FDTD and can be duplicated over the whole lattice by applying phase equivalent to lattice constant variation $\exp(jka)$ with the help of Bloch's theorem [29].

There are some variations of FDTD method proposed for faster computation of problems. First of all, it is possible to shorten simulation time by restricting the problem

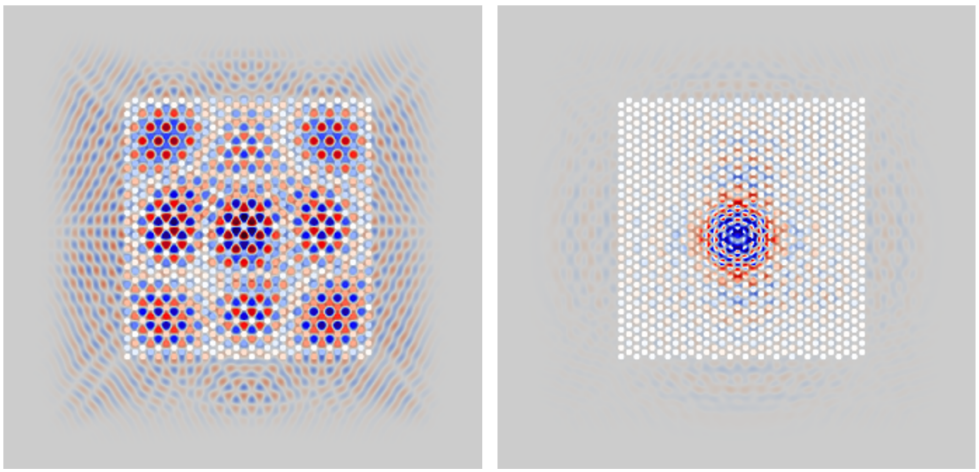

Figure 3.2: Example electric field distributions simulated by FDTD method showing a photonic crystal that modes are transversely excited. Perfectly matched layers (PML) are used as boundary conditions. The laser beam width is shown for Left: dielectric band mode and Right: band gap. The excited Bloch mode can be observed for dielectric band mode while the beam remains confined due to lack of modes in the gap.

into lower dimensions by eliminating invariant ones. 2-D FDTD method is such one that restricts the problems such as one dimension is either constant or infinite comparing the others, into two dimensions. For similar structures, there is another hybrid approach called 2.5-D FDTD. This method is mostly used for planar photonic integrated circuit calculations. The 3-D simulation domain is projected into 2-D via effective-index method by calculating effective index along the nearly-invariant direction given that there is little coupling between different slab modes [31].

In this study, a commercial FDTD package named MEEP is used [32]. It is capable of solving Maxwell equations in 1-D, 2-D and 3-D. The solved medium can be anisotropic, dispersive or nonlinear. The boundary conditions can be used are PML, absorbers, PEC's and periodic boundaries. It is capable of computing transmission spectra whose example given in Figure 3.3, resonant modes and field distributions in Figure 3.2. In order to increase numerical stability and handle smooth edges of

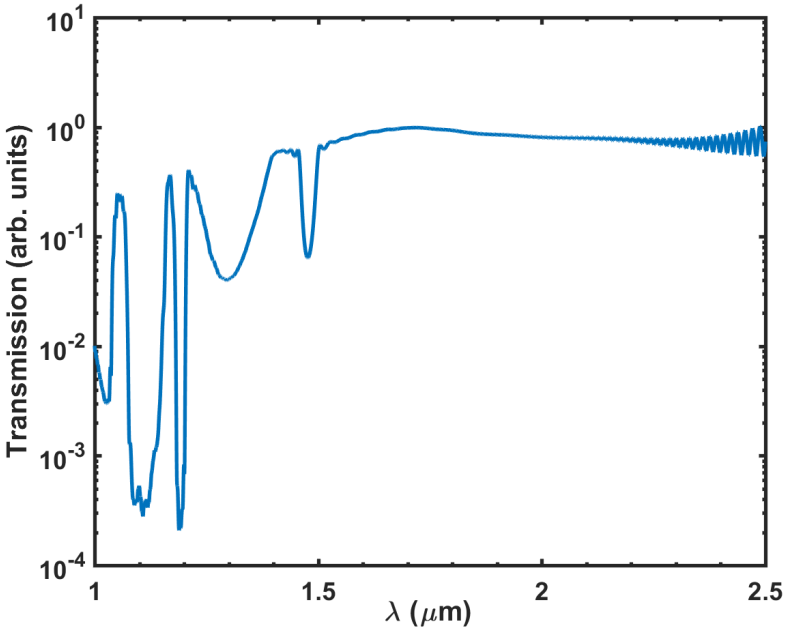

Figure 3.3: An example TM transmission spectrum of a Si photonic crystal with 220 nm thickness 110 nm hole radius and 670 nm lattice constant is given. Here, the crystal is excited with a line source having Gaussian spectral linewidth. The transmissivity for each frequency is obtained internally with an Fourier operation [32].

structures such as curves, it employs subpixel averaging, which is assigning permittivities on each grid point by averaging the permittivity composition inside that grid cell. This enables the gradual change at the dielectric-contrast interfaces instead of step-index changes.

3.2 Plane-wave Eigensolvers

The second method used in this study is plane-wave eigensolvers. Solving eigenmodes of a photonic crystal is a frequency-domain problem in its nature. Thus, this method approaches to the problem in a plane-wave basis. The periodic lattice can be decomposed as Fourier series with a period of a. The result of the analysis is the sum

of the components at every reciprocal lattice vector $\vec{G}$, as it is shown at Section 2.3.

$$f_k(\vec{r}) = \sum_G a_G(\vec{k}) e^{j\vec{G}\cdot\vec{r}} \tag{3.6}$$

In this problem, it is important to compute coefficients a_G for each reciprocal vector. In our problem, the periodic function $\vec{f_k}(\vec{r})$ is corresponding to E and H vector fields. Thus, the coefficients should also be vectors. The periodic functions should also satisfy the transversality constraint, $(j\vec{k} + \nabla) \cdot \vec{f_k} = 0$. The form of the constraint applied to the case above provides the following equations [2].

$$(\vec{k} + \vec{G}) \cdot \vec{a}_G = 0 \tag{3.7}$$

This condition is satisfied by constructing the fields as plane waves. In that way, two coefficient vector can be chosen and their superposition can be inserted to eigenvalue equation. Inserting the necessary elements to the eigenvalue equation and Fourier transform the both sides of it, it is obtained that;

$$\sum_G [-\varepsilon^{-1}_{G'-G} \cdot (\vec{k} + \vec{G'}) \times (\vec{k} + \vec{G}) \times] \vec{a}_G = (\frac{\omega}{c})^2 \vec{a}_G \tag{3.8}$$

The left hand side of the equation is an infinite sum for infinite set of reciprocal vectors. In order to compute numerically, the number of the vectors must be truncated. In order to exclude larger terms of reciprocal vectors, the permittivity distribution over the medium undergoes discrete Fourier transform for discretization and approximation. This helps reducing the sum to a finite set. With the help of FFT and iterative methods, the eigenvalues for each component are computed [2].

The package used in this study as eigensolver is MIT Photonic Bands (MPB) [33]. It is capable of simultaneously solving eigenfrequencies and eigenmodes with a direct, frequency domain approach. It is capable of computing the modes around a specified frequency or solving iteratively for each wavevector. It offers easier generation of band (Figure 2.2) or equifrequency diagrams (Figure 3.4).

3.3 Further Methods to Solve Photonic Circuits

There are other methods for photonic integrated circuit simulations that are not in the scope of this study. However, such methods are very essential for the progress of these efforts in future.

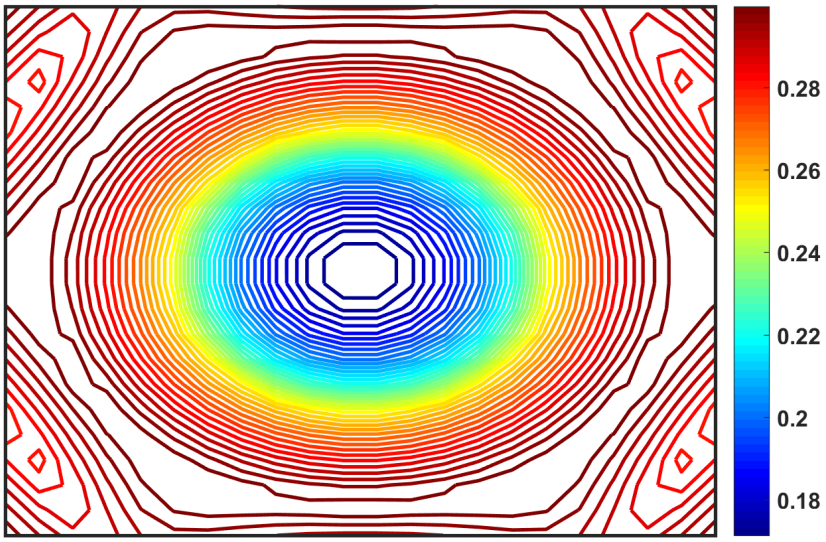

Figure 3.4: TM equifrequency contour diagram of the second band of a photonic crystal with $h/a = 0.744$ and $r/a = 0.279$. It allows us to analyze possible wavevectors at symmetry axes of the lattice for each frequency.

3.3.1 Beam Propagation Method

The first one of such methods is beam propagation method. It is most suitable for solving slowly varying structures that paraxial approximation can be applied [31]. In this method transverse electric field at a given position is decomposed into its constituents through Fourier transform as monochromatic plane waves in the form of $\phi(k) = A_i \cdot e^{jk_i \cdot r}$. Each constituent is propagated by a finite step for an average refractive index. Then, the decomposition is multiplexed through inverse Fourier transform, in order to obtain superposition in time domain [34]. In order to correct computational errors on the phase front in the earlier stage, spatial perturbations are applied in proportion to local refractive index variance in the form of $\Delta\Phi(x, y, z) = e^{jk_0(n-\bar{n})\Delta z}$ at every finite step.

It can be expressed that the form of wave function at the end of each finite step Δ_z as given in (3.9) [34].

$$\Psi(x, y, \Delta z) = \frac{e^{j\bar{n}k_0\Delta z}}{2\pi} \int_{\beta>0} \Phi(k_x) \exp\left[\frac{-jk_x^2}{n\bar{k}_0 + \sqrt{\bar{n}^2k_0^2 - k_x^2}}\Delta z\right] dk_x \tag{3.9}$$

3.3.2 Eigenmode Expansion Method

A similar method is eigenmode expansion, which decomposes local field into constituent modes. These modes are propagated individually for further superposition. When field reaches a section having different properties, interfacing is done through S-parameter calculation between two sections [31] .

CHAPTER 4

WAVE PROPAGATION IN AMORPHOUS MEDIA

4.1 Electron Behavior in Amorphous Semiconductors

4.1.1 Electronic Band Theory

The behavior of electrons inside the semiconductor crystal are very similar in nature to the photon behavior inside photonic crystals. It is known that, electrons show wave-like properties, thus the rules of wave mechanics apply [2]. Since the governing Schrödinger equation (4.1) has a very similar form to the wave-equations that are given in (2.9) and (2.10), postulates on Schrödinger's equation can be implemented on photonic crystal structures. This section is important because studying amorphous semiconductors may provide insight for our amorphous photonic material studies.

$$[\frac{-\hbar}{2\pi}\nabla^2 + V(r)]\psi_E = \hat{H}\psi_E = E\psi_E \tag{4.1}$$

It was discussed earlier that, for the solution of Maxwell's wave equation, the lattice can be reduced with respect to symmetries in the periodic refractive index variations. Bloch's theorem is very essential in reducing the dispersion relation to the irreducible Brillouin zone. The periodic function for the Schrödinger's equation, lattice potential also can be reduced in to IBZ with the help of Bloch's theorem. The analysis of lattice is the same as photonic crystals'; however the IBZ's are mostly three dimensional for semiconductors. In these crystals, the electron wave propagations are subjected to Bragg reflection phenomenon [2]. The Bragg condition inside the crystal is:

$$(\vec{k} + \vec{G})^2 = \vec{k}^2 \tag{4.2}$$

This condition expresses that the different wavevectors must be degenerate over the Brillouin zones. Solutions of Bragg condition provide standing waves over the zone, whose interference creates forbidden states, i.e. band gaps. The extent of band gap can be inferred from optical absorption spectra, carrier concentrations, Fermi level and temperature dependency of the lattice conductivity [23].

In order to compute the band structure of a semiconductor crystal, two models can be used. As a first approach, the nearly free electron model is suitable. In this model,the electrons in the lattice have eigenvalues of a free electron, but are perturbed weakly by a periodic potential V(r). This perturbation causes the formation of band gaps around the Bragg scattering planes [3].

As a second approach, tight binding approximation can be utilized [35]. It is based on the assumption that wave functions of neutral separated atoms overlap inside the lattice. According to this approximation, the electrons must have limited interaction with the energy states of the surrounding atoms. This enables electron behavior to be expressed by atomic behavior. The linear combination of overlapping wave functions forms two new wave functions, an attractive and a repulsive one. When multiple atoms get closer enough, the energy states start to split into bonding and antibonding states. Among them, the degenerate ones form bands in the band structure which also create a band gap between two consecutive bands [23].If this approximation is explained mathematically, the wave function can be identified as:

$$\psi_k(r) = \sum_i C_{k,i}\varphi_i(r - R_i) \tag{4.3}$$

$$C_{k,i} = N^{-1/2}e^{ikR_i} \tag{4.4}$$

where $N^{-1/2}$ is the normalization factor for a N-atom crystal. $C_{k,i}$ here is making the wavefunction as Bloch-type. The energy eigenvalues for the structure can be computed by the Hamiltonian [23].

$$E(k) = \langle k|H|k\rangle = N^{-1}\sum_i\sum_j e^{jkR_i - R_j} \times \int \varphi \cdot (r - R_i)H\varphi(r - R_i)d^3r \tag{4.5}$$

Let us simplify the equation by considering relative distances $R_m = R_i - R_j$

$$E(k) = \sum_m e^{jkR_m} \int \varphi(r - R_m)\varphi(r)d^3r \tag{4.6}$$

Further simplification can be done by considering only the terms which $R_m = 0$ and the contribution of nearest neighbors with R_n. This reduces the problem only to the nearest overlapping functions instead of the whole lattice.

$$\int \varphi^*(r)H\varphi(r)d^3r = -A \tag{4.7}$$

$$\int \varphi^*(r - R_n)H\varphi(r)d^3r = -B \tag{4.8}$$

$$E(k) = -A - B\sum_n e^{jkR_n} \tag{4.9}$$

4.1.2 Effect of Disorder and Band Tail Characteristics on Amorphous Semiconductors

For a semiconductor lattice, the band gap and extended modes are separated by the mobility edge. The density of available electronic states are zero in the band gap region for an infinite lattice. The mobility edge can easily be identified by the Van Hove singularities in the density of states [27]. When disorder or defects are induced into the lattice, the periodicity is disturbed. Thus, the postulates of Bloch's theorem becomes invalid. As a result, the defect modes are introduced into the band gap, which are also localized. The singularities at mobility edges of valence and conduction bands disappear. Enough accumulation of such localized modes creates tail states that enable the electron presence inside the band gap region. These are called as band tail [36, 37].

For a complete amorphous semiconductor such as a-Si, the density of states at band gap region is nonzero. The mobility edges here have the duty to separate the localized and extended modes, i.e. bands and band tails. These band tails have exponential characteristics and affect the electrical and optical properties of the semiconductor, which are largely dependent on the density of states. The absorption spectra and DC conductivity are some of the examples [37]. The optical absorption edge of the semiconductors are governed by the Urbach rule [38]. The general rule specifying absorption characteristics are provided in (4.10) [37]. Here, α_0 and E_0 are material

specific constant, while E_U is called as Urbach energy which the main parameter determining the slope of the absorption edge.

$$\alpha(h\nu, T) = \alpha_0 \cdot exp[\frac{h\nu - E_0}{E_U}] \tag{4.10}$$

The Urbach energy E_U is highly depending on different disorder factors. This dependence can be summarized as,

$$E_U = (E_U)_T + (E_U)_X + (E_U)_C \tag{4.11}$$

The equation (4.11) relates the Urbach energy with temperature disorder (T), structural disorder (X) and compositional disorder (C). The temperature disorder originates from the thermal fluctuations, while structural disorder is due to defects and randomness in the lattice and compositional disorder is valid for mixed lattices with various atomic compositions [37].

For amorphous materials, the main characteristic is a smeared and extended tail with exponential behavior. In this case, localizations due to randomness in the structure cause the slope of the optical absorption to be structural-randomness dominant and less reliant on the temperature-dependent fluctuations especially in the materials that at lower temperatures and having only short-range order [37]. Another important property is for the valence and conduction band tails, the slope parameter E_U is different. This means that two band tails on the opposite sides of the band gap are affected by randomness by different degrees.

The importance of Urbach tails is that the optical absorption edges are one of the most obvious observables for state densities. They possess an intuition to analyze the effects of randomness. In order to analyze the density of states directly, the Schrödinger equations need to be solved. The analysis of the density of states on amorphous semiconductors is done using tight-binding approximation, whose principles are explained briefly before. The initial studies of Drabold et.al. [39] describe the localized-to-extended state transitions which are known as Anderson transitions, based on the seminal work of Anderson [40] examining the electron localization in a disordered medium. An a-Si model with 512 atoms generated by Djordjevic et. al. [41], is used to calculate the density of states via tight-binding approximation and verified by DC conductivity analysis and inverse participation ratio calculation, which

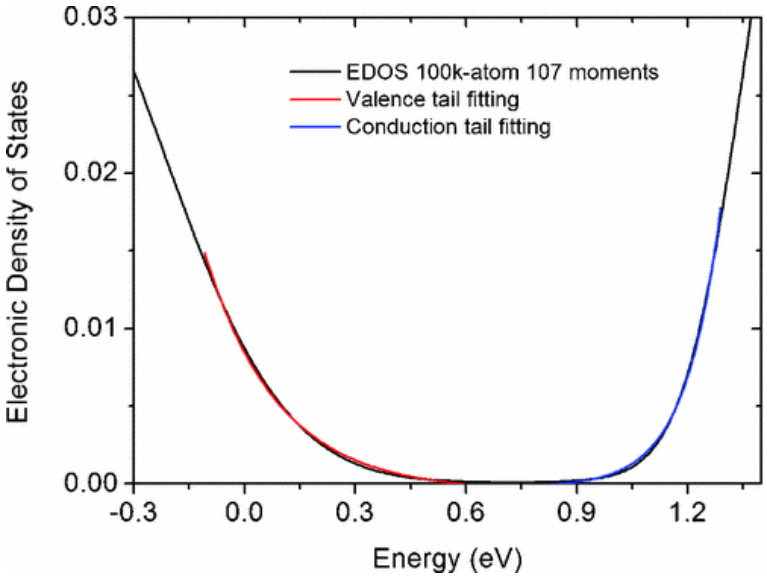

Figure 4.1: The density of states spectrum for amorphous silicon simulated from a model with 100k atoms [41, 42]. The conduction and valence band tails are fitted exponentially. It can be seen that valence band tail slope is smoother than conduction band tail slope. Reprinted figure with permission from [42] (doi:10.1103/PhysRevB.83.045201). Copyright (2018) by the American Physical Society.

is an indicator of degree of localization. In this work, the localization of the states at the energies around the band tails are shown as decreasing while approaching the mobility edge. This is due to the formation of weakly overlapped states of the same energy which form the extended states at enough overlap, which is also the indicator of the mobility edge. Moreover, it is shown that there is a slope difference between exponential characteristics of valence and conduction band tails.

A theoretical study with same model shows that the band tail states are in fact, very delocalized [43]. Such state functions cover a couple of atoms which are weakly coupled with each other. In this work, the valence tail states are shown to be statistically identified with short bonds inside the lattice while the conduction tail states are lying over longer interactions. It is known before that, the Urbach energy determining the tail slope for the valence tail is more structural disorder dependent, while the conduction tail slope is less affected by structural variations but more affected by the temperatural effects [44]. In a later work over the bond dynamics in a-Si with a larger

model, the reason of this tendency is connected with the bond length [42]. Since the valence band tail is associated with the short bonds, such bonds are more susceptible to structural variations in a short range, while conduction tail states are overlapping over a longer range and thus, less affected by the disorder. In order to get a better idea, the band tails of a-Si generated through tight-binding simulations of a domain with 100k atoms is given in Figure 4.1 [42].

The importance of this conclusion is that it suggests the asymmetry between band tails is related to the connectivity of tail states. The overlap range between the states of similar energy affect their susceptibility to disorder and structural variations. Since localization is a result of wave-mechanical nature, it is not just confined to Hamiltonian. Such a correlation can be searched in other domains such as a classical EM wave, as will be attempted in later sections.

4.2 Wave Propagation in Disordered Lattices

The waves in free space can be described as a plane wave having a definite frequency and propagation direction. However, when the wave encounters a disordered medium consisting of independent scatterers, this behavior is altered by the multiple scatterings. Two types of scatterings are capable of altering the wave propagation. Elastic scatterings are the events where the energy (or frequency) is preserved, however the propagation direction (i.e. its wave-vector, $\tilde{k}$) changes. On the other hand, inelastic scatterings have destructive effects on both the frequency and the wave-vector. Depending on the scattering medium, the mean length at which the coherence of the wavefront is preserved changes. This scattering-free mean length is heavily dependent on the R/λ ratio, which is the ratio of scatterer size to wavelength. If the wavelength is a lot larger than scatterers, the wave undergoes weak scattering, since scatterers are at sub-diffraction length. Thus, the wave sees a homogeneous effective medium. On the contrary, when wavelength is significantly smaller than scatterers, the wave is capable of resolving the medium, so it cannot sense the variations in the lattice. The important case is when both the scatterers and the wave are comparable. In this case, multiple scatterings accumulate over distances longer than scattering-free length and disturb the wavefront. This kind of wave transport is known as diffusive

transport. This behavior is very similar to the Brownian motion of a classical particle. Nevertheless, there are some characteristic differences between classical and wave diffusion due to different natures [45].

When the waves undergo multiple scattering, it is expected that the phase front is lost after a distance greater than scattering-free length. From a classical perspective, smooth variations of the intensity at the phase front are expected. Nevertheless, this is not the case. In the event of wave scattering, a speckle pattern with bright and dark spots is observed due to mutual interference of the scattered wave. This pattern is dominant when there is no inelastic scattering. The reason of this difference is the phenomenon of "coherent backscattering". As a result of this phenomenon, under the presence of disorder in a medium, the wavefront that undergoes multiple scattering is still phase coherent, however in the opposite direction. Due to this coherence, there is a constructive interference among the wave, so the backscattering probabilities increase further. As a result of coherent backscattering, the diffusion constant of the wave decreases, so a need to renormalize the diffusion constant arises. Coherent backscattering effect is evidenced by multiple studies in 1980's and well accepted now [46, 47, 48].

The angular profile of the backscattering is heavily influenced by the rules of wave interference [45]. This profile can be obtained by averaging the field amplitudes at different configurations with the same level of disorder, since the phase of the wave will be different for each configuration, which causes them to cancel themselves out, leaving only the backscattering effect. The angular profile is independent of time and has time reversal symmetry for appropriate media, which means there is a reciprocity between incident and scattering wave vectors. Furthermore, coherent backscattering is independent of the path taken between initial and final scatterings, and the intermediate steps cancel out. The path evolution for a scattered light can be expressed as equations 4.12 and 4.13 and shown in Figure 4.2. Here n denotes scatterers while G is the scattering strength on the phase relation. Notice that for another wave B_0 along the same route with inverse order is capable of canceling the former [45].

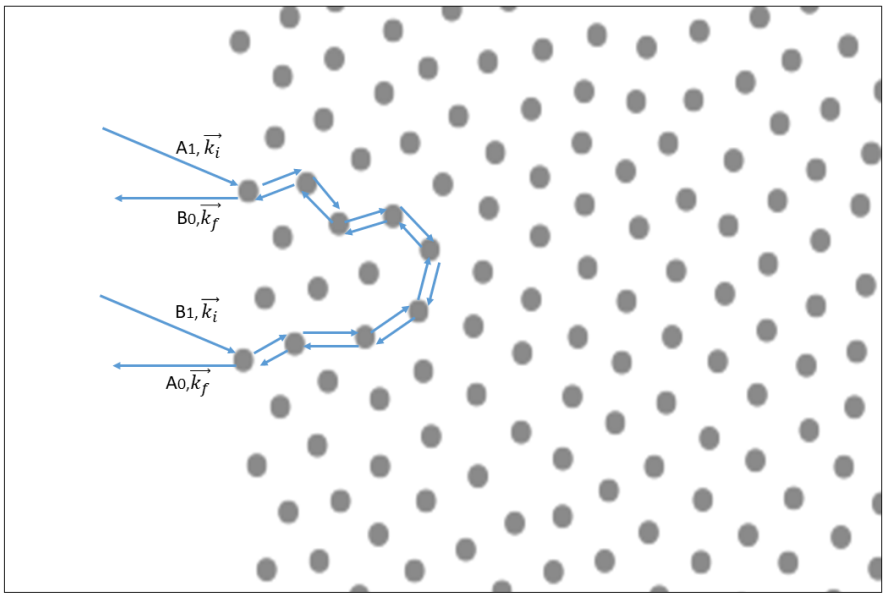

Figure 4.2: The scattering path of a wavefront inside a random media is given as an example. If the media has time reversal symmetry, the intermediate paths for two scattered waves A_0 and B_0 destructively interferes with each other. Coherence of waves are only dependent on initial and final wavevectors.

$$A_0 = A_i G \exp[jk_i \cdot (r_1 - R_0) + jk_{1,2} \cdot (r_2 - r_1) + ... \\ + jk_{n-1,n} \cdot (r_n - r_{n-1}) + jk_f \cdot (r_0 - r_n)] \quad (4.12)$$

$$B_0 = B_i G \exp[jk_i \cdot (r_n - R_0) + jk_{n,n-1} \cdot r_1) + ... \\ + jk_{n-1,n} \cdot (r_n - r_{n-1}) + jk_f \cdot (r_0 - r_n)] \quad (4.13)$$

Examining the equations and Figure 4.2, one can say that the coherence of the incident and scattered wave is only depending on the wave vectors k_i and k_f. In the case of $k_i = -k_f$ these waves are perfectly coherent. For a lattice, there are many scattering paths between r_1 and r_n. So, the assumption of time reversal symmetry inside the lattice postulates that for every scattering path, there is a time-reversed version of that path with same scattering order. So, in the presence of disorder, the phase difference between two scattered waves A_0 and B_0 is only depending on initial and

final wavevectors. Thus, for a coherent incident wave, the backscattering will also be coherent [45]. This relation is given below in (4.14).

$$\frac{A_0}{B_0} = \exp[j(k_i + k_f) \cdot (r_1 - r_n)] \tag{4.14}$$

The angular profile of backscattering depends on the incident and final scattering wavevectors. For the basic two path system, it can be summarized as in (4.15).The angle between incident and scattered waves diminishes the backscattering probability i.e. intensity, but is not become zero immediately. The backscattering profile can be obtained by averaging over many different configurations with same statistical properties. Since the phenomenon is path independent, the exact configurations of scatterers are not important due to the cancellation of other terms in the interference formula [45].

$$|A_0 + B_0|^2 = |A_0|^2 \cdot \{1 + \cos[(k_i + k_f) \cdot (r_1 - r_n)]\} \tag{4.15}$$

There are some important points in coherent backscattering regarding to sample size. In order for backscattering to occur, the minimum sample size should be at least one scattering free length. When the lattice length is increased beyond it, the scatterings accumulate and increase the coherent backscattering probability,since the possible intermediate paths that light can scatter will be much more.

The coherent backscattering is seen as a precursor of wave localization. When backscattering probabilities are too high under strong disorder, the diffusion constant of the wave will become zero. In this case, the wave can be considered as 'localized'. This phenomenon was first explained by Anderson in 1958 to describe the disappearance of electron diffusion under strong randomness of lattice potentials in the absence of electron-electron interactions [40]. Later Anderson localization model was extended to classical waves by analyzing photon transport inside GaAs powders [49].

Classical waves are very beneficial in understanding the localization phenomenon stemming from absence of inelastic scattering in contrast to electrons. It is explained further by the scaling theory of localization, which postulates that the localization model is independent of lattice type and properties. The most important indicator is dimensionless conductance, which is a measure of how the wave state extent changes

with sample size. Another issue is that the localization is dependent on the dimensions of the lattice. It is postulated that, all waves are localized in one and two dimensional systems without taking into account the degree of randomness when sample size goes to infinity [50]. This means that an extent can always be found for the state that can be considered as localized, except three-dimensional cases. In 3-D, the extended and localized states can occur together but at different frequencies. The limit that separates this two behavior is named as mobility edge, in this context.

The dimensionless conductance γ is defined as the ratio of eigenvalue change due to the variances in boundary condition to the average difference between two consecutive eigenvalues, $\gamma = \delta\omega/\Delta\omega$. Here, the average difference $\Delta\omega$ should change with L^{-d}, with d is dimension and L is sample size [45]. However the sensitivity of eigenvalue to boundary changes such as increase in sample size, $\delta\omega$,is depending on the localization. If the mode is localized, the state can sense the boundary changes up to extent of its exponential tail, while the extended states would always sense the change. Due to this, there is a scaling function defined to analyze the relation of conductance with the change in sample size, which is $\beta = \frac{d\ln\gamma}{d\ln L}$.

$$\beta \propto \begin{cases} d-2, & \gamma >> \gamma_c \\ ln\gamma, & \gamma > \gamma_c \\ 0, & \gamma = \gamma_c \end{cases}$$

This shows that, at critical conductance level γ_c, the state becomes independent on the sample size, which one expect from the localized states. However, in this formula, the scaling function seems only dependent on dimensionless conductance, but the effect of the randomness of scatterers is ignored. For this, the change in randomness of the lattice, which is indicated by the localization length normalized by the sample size ξ/L. It means that, for every degree of randomness, there is an extent that the wave becomes localized [45, 50]. The localization length can be calculated for 2-D materials with the formula $\xi = l * \exp(\kappa_e l\pi/2)$ that has an exponential behaviour, which causes large increase at lower level of randomness. For three-dimensional random lattices, the condition determines the mobility edge and signaling localization is given as $\kappa_e l \leq 1$ and known as Ioffe-Regel condition. It means that if scattering free mean path is comparable to wavelength, wave lost its wavefront and bound to localization [45, 51].

Another form of explanation for the localization phenomenon of light in 2-D lattices is proposed by Raedt et.al. in 1989 [52]. According to this transverse scheme of light localization, if the refractive index variations are random over x-y plane but it is constant in the z direction, the diameter of light beam propagating at z direction may only increase until localization length scale and remains confined. In the transverse localization regime, the wave evolution is explained by paraxial approximation.Here ψ is envelope of the propagating field with ω and k. Δn indicates the local refractive index variations over average index. The equation is very similar to time-varying Schrödinger's equation, thus it can be said that the wave is like a quantized particle inside random potential. Transverse localization is addressed later in 2-D photonic materials with random index variations by Schwartz et.al. [53]. Later, it is used to control light propagation at sub-wavelength scale to ensure hyper-collimation [54].

$$j\frac{\partial\psi}{\partial z} = [-1/2k(\frac{\partial^2}{\partial x^2} + \frac{\partial^2}{\partial y^2}) - \frac{k}{n_0}\Delta n]\psi = H\psi \tag{4.16}$$

CHAPTER 5

GENERATION OF AMORPHOUS CONFIGURATIONS

5.1 Theory of Importance Monte Carlo Sampling

Monte Carlo simulations are basically simulations that involves random numbers in the algorithm. These algorithms do not follow a predefined, deterministic flow along the simulation; rather, the system is evaluated in a stochastic way. They have a very wide range of applications from chemistry and physics to finance and biology. The stochastic nature of Monte Carlo simulations are very suitable to checking hypothesis via some random inputs or making efficient calculations with lesser statistical error. Moreover, Monte Carlo simulations are one of the two methods that are used to analyze thermodynamic properties of molecules with molecular-dynamics simulations.

Different from Molecular Dynamics simulations, Monte Carlo algorithms do not require any force calculation and thermostats to control thermodynamic properties.The only thing matters is the energies of the constituents of domain. Moreover, the time progression in such algorithms are not linear and sequential; rather the progression is random. Thus, there is no numerical inaccuracy due to discrete time approximations [55].

One of the basic applications for Monte Carlo method is sampling to compute an integration. In a molecular simulation, the statistical thermodynamic properties of a system is considered to be extracted from a partition function in equilibrium, which is given at (5.1). H, stands for Hamiltonian or total energy of the system at each state, while k_B is Boltzmann constant and T is temperature [56]. This function is the sum of all possible states in a system and scales by the degrees of freedom. Once the partition function is determined, it is possible to compute all observables of the

system as specified in (5.2) .

$$Q = \int e^{-H(r^N, p^N)/k_B T} dr^N dp^N \tag{5.1}$$

$$\langle A \rangle = 1/Q \cdot \int A(r^N, p^N) e^{-H(r^N, p^N)/k_B T} dr^N dp^N \tag{5.2}$$

Normally, numerical computation of such a N-dimensional integral given in (5.2) is done via sampling the equation in an equidistant manner. In this method, in order to decrease the numerical errors, the grid must be as fine as possible with very high sampling rates. For small dimensions, this may seem as efficient; however the computational complexity scales with mesh, exponentially. Moreover, the contributions to integral at the sampled points have a good chance to be negligible along a uniform mesh, due to the differences in concentration of the function [56]. To solve these inefficiencies and decrease numerical errors, Monte Carlo sampling is proposed [57]. Via Monte Carlo sampling, instead of a fixed grid, the function is sampled at random points in the configurational space, which is the matrix of all possible states. In this way, it is possible to calculate the observable with lesser amount of samples and smaller error. However, in this case the distribution of random samples is very important so that the result is very accurate. So, an optimized algorithm to an efficient random sampling which minimizes the numerical error is proposed by Metropolis in 1953 [58]. The algorithm is basically assigns importance to every sample according to contribution of it to the result of the integral. The most important samples are included in the result while the samples with least contribution is discarded, with a probability in both cases.

It is indicated before that, the partition function Q, possesses all the information about all possible configurations. To calculate the probability of occurrence of a given configuration, first the configuration is separated into dependent parts of Q with the notation of $Z = \int e^{-H(r^N)/k_B T} dr^N$ [56]. Among whole states, occurrence probability of a particular state can be identified as,

$$N(r^N) = \frac{\exp\left(-H(r^N)/k_B T\right)}{Z} \tag{5.3}$$

In the Metropolis algorithm, a random walk is conducted to determine the samples with largest contribution to the result. Let us take into account two states, 1 and 2. Their occurrence probabilities are specified by Boltzmann factors as N(1) and N(2), calculated via (5.3). The walk is done between two states by trial and error; i.e. at every transitional move, the effect of move on the state is examined and the move is accepted with a transition probability $\pi(1 \rightarrow 2)$ according to the result. In order to preserve the equilibrium along the configuration, the movements must be in balance. Thus, the average effect of the large number of accepted moves must be negated by reverse movements from state 2 to 1. This condition is named as "detailed balance condition" which is given at (5.4) [56].

$$N(1)\pi(2 \rightarrow 1) = N(2)\pi(1 \rightarrow 2) \tag{5.4}$$

The transition probability specified in detailed balance condition has two components, the probability of occurrence for such a trial move between states 1 and 2, and the acceptance probability of this trial move. The random nature of both is considered as essential for Metropolis method. Regarding the occurrence probability, for the Metropolis method, the given matrix is selected as symmetric, which means equal probabilities for selection of a move from state a to b and vice versa [56]. Thus, the detailed balance condition can be reduced to the (5.5).

$$N(1)acc(1 \rightarrow 2) = N(2)acc(2 \rightarrow 1) \tag{5.5}$$

$$\frac{acc(1 \rightarrow 2)}{acc(2 \rightarrow 1)} = \frac{N(2)}{N(1)} = e^{-[H(2)-H(1)]/k_B T} \tag{5.6}$$

The rewritten form of the equation (5.5) in (5.6) indicates that the ratio of acceptance probabilities is depending on the ratio of Boltzmann factors describing the corresponding states. To satisfy the detailed balance condition, it is essential to select a suitable acceptance probability distribution. Metropolis algorithm defines this probability as given below. According to definition, when the new state 2 has more energy then the current state 1, there is a probability to accept such a movement which is given in (5.7). However, when the reached state 2 possesses less energy than the initial state 1, this kind of movements are always accepted, with a probability of 1. So, the system tends to relax itself to lower energy levels [56]. This kind of processes are

known as Markov processes, or Markov chains, which are stochastic processes that the future move is only depending on the present state, no matter how was the past.

$$acc(1 \to 2) = \begin{cases} N(2)/N(1), & N(2) < N(1) \\ 1, & N(2) \geq N(1) \end{cases} \tag{5.7}$$

For molecular simulations, in order to construct the Markov chain, the algorithm of Metropolis method is as follows [56].

1. First, an element in the configuration is selected randomly and its present energy H(1) is computed.

2. The element is displaced by a random amount, and the energy in the new state, H(2) is computed.

3. The acceptance probability of the move is calculated according to (5.7). A random number from uniform distribution between zero and one is selected and if it is smaller than the calculated probability, the move is accepted and added to the end of the Markov chain.

The algorithm and the underlying principles are explained previously. The simulations with Metropolis algorithm for importance sampling over a thermodynamic system need some mechanisms that enable replication of real-world conditions. First of all is determination of a simulation boundary condition to restrict the problem to a finite and solvable cell without introducing errors. The size of simulation cell depends on the purpose of generated amorphous configuration. Here, the choice is using periodic boundary conditions [56]. By applying periodic conditions, an infinite domain is created by duplicating the initial system. This new domain is immune to the boundary effects. For example, when a random displacement is applied, if the particle goes out of the computed domain, its image will be entered to the system from the opposite wall due to periodicity. This property is very useful to conserve number of particles inside the domain.

Another issue in this case is, one particle does not only interacts with the other particles in the cell, but also interacts with their images at other periodic cells, which is a drawback that makes the sampling an infinite sum. To handle that, a truncation is

applied to interactions that neglects the ones that has least amount of impact. This can be done in two ways. The most basic way is to use a piecewise function taking zero value outside a radius r_c. Assuming this will create a discontinuity at the cutoff value, which may or may not be important depending on application. If it is wished to avoid discontinuities, another method is used that involves both truncation and shifting of the potential with respect to the cutoff radius r_c. In that case, the discontinuity is eliminated by subtracting the excess amount of energy to make potential vanish at cutoff [56].

$$U(r) = \begin{cases} H(r) - H(r_c), & r \leq r_c \\ 0, & r \geq r_c \end{cases}$$

An important thing when Metropolis sampling is done over a thermodynamical system is, in order to compute system properties, some assumptions and idealizations are done to predict equilibrium conditions. These are called as thermodynamic "ensembles" and play huge role during computations. Basically, while conducting Monte Carlo simulations, some properties of the simulation domain such as particle count, volume, temperature pressure, density etc. are considered as constants at equilibrium. Among the most common thermodynamic ensembles, the canonical ensemble (constant particle count N, volume V, and temperature T, known as NVT), microcanonical ensemble (constant N, V and energy E), isobaric-isothermal (constant N, pressure P and T) and grand canonical ensemble (constant chemical potential μ, V and T) can be counted. The Metropolis algorithm is subjected to changes according to selected ensemble for different types of simulation domains [56].

The most widely used ensemble is canonical ensemble, which is also the case for amorphous configuration generation in this study. In a canonical ensemble of amorphous material, the number of scatterers is constant throughout the Metropolis sampling process. This is ensured by the application of periodic boundary conditions. During the simulation, the volume of the domain and the equilibrium temperature is kept constant.

Another important issue is the calculation of Boltzmann factors for acceptance probability. It is indicated that the Boltzmann factors are directly proportional with the Hamiltonian of the configurations. Thus, it is essential to find the best model that imitates the properties of simulated system. Thus, potential energy function models

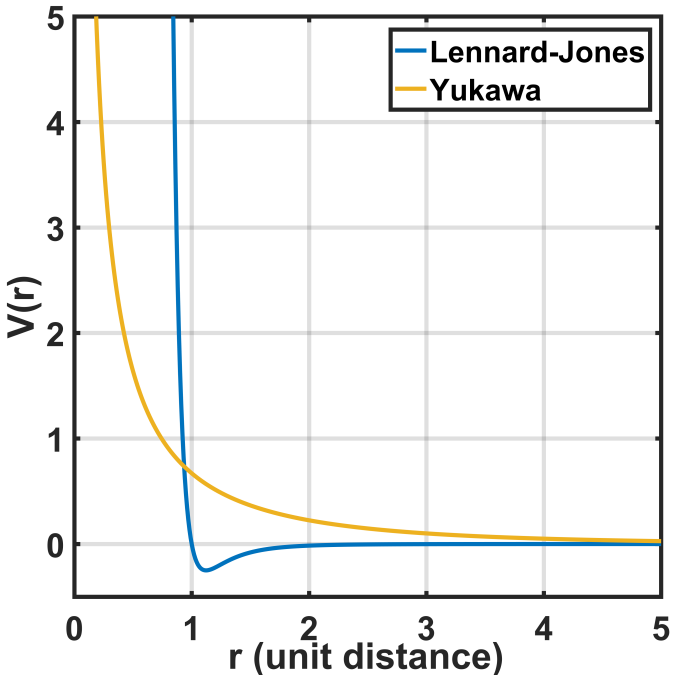

Figure 5.1: Curves of Lennard-Jones and Yukawa potential energy functions with generic coefficients are provided.

(PEF) are widely used for this purpose [59]. These models enable the computation of pairwise interactions in a lattice approximately and the determination of the equilibrium conditions. There are various potential energy functions defining pair or multi-body interactions which are taking the lattice angles into account additionally. Most of them are parametrized empirically for different case studies. For example, one of the most popular potential energy functions is Lennard-Jones potential, which is a simple pairwise function that incorporates both attractive and repulsive forces. The function is given at (5.8), while the potential curve is provided at Figure 5.1. The main characteristics of the potential profile is determined by two parameters, ϵ and σ. The former is determining the absolute minimum of the potential energy, while the latter is the point that the pair potential between two scatterers is zero [56].

$$U_{LJ}(r) = 4\epsilon[(\frac{\sigma}{r})^{12} - (\frac{\sigma}{r})^{6}] \tag{5.8}$$

Another type of potential that is also extensively used in this study is Yukawa potential, whose characteristics are given at (5.9) and Figure 5.1 [60]. It is first proposed by Hideki Yukawa in 1935 to model mesonic interactions and the nuclear forces in-

volved [61]. The utilization of Yukawa potential then extended to particles in plasmas and charge-stabilized colloids [62]. The Yukawa potential has a very short effective range, so it is beneficial to generate long-range uncorrelated, stabilized structures. The form of Yukawa potential is given at (5.9). Here, ν_0 is a scaling constant, which is often normalized, and l is screening length of the potential. The cutoff length r_0 is an important parameter determining equilibration speed and accuracy. It is concluded that at the reduced length value of 3.5, i.e. 3.5 times of lattice constant is sufficient for accurate results [61].

$$U_{Yukawa}(r) = \frac{\nu_0}{r} \exp(\frac{-r}{l}), r < r_0 \tag{5.9}$$

5.2 Implementation of Metropolis Algorithm to Generation of Amorphous Configurations

In the scope of this study, it is essential to generate an equilibrated configuration of scatterers which does not possess a long range order, i.e. periodicity, but a short-range relation. For an amorphous slab comprising scatterers like holes or rods, it is convenient to take them as 2-D hard disks or point particles over x-y plane, since z-plane is invariant. The flow of the simulation for a 2-D amorphous photonic slab is similar to mentioned in previous section and provided below.

1- An initial configuration is given. It can be a periodic photonic crystal slab configuration with hexagonal or square lattice. This helps to predict the transport properties of the resulting structure. Alternatively, a previously generated amorphous configuration can be inserted for quicker equilibration. The distribution of the initial configuration is not important for the equilibrium. Here, the important point is, the configuration is considered as a distribution of particles over a liquid-like structure [18], which resembles a colloidal interaction. Calculate the potential energy of the configuration. While conducting potential energy calculations, it is essential to pick the correct ensemble. In this case, canonical ensemble (constant NVT) is used.

2- Select a scatterer randomly from the distribution, and apply a random displacement on it. The maximum extent of the displacement is adjusted by trial to get an optimum acceptance rate. Acceptance rate is the determining factor for the time required for

equilibration. In this study, it is preferred as 40% - 60%. Calculate the new potential energy.

3- The acceptance of the displacement depends on the probability calculated from Metropolis criterion: $acc(1 \rightarrow 2) = min(1, e^{-[U(2)-U(1)]/k_B T})$

Repeating the random displacements over a large amount of steps equilibrates the structure. There are some measures of equilibrium statistics. First, along the simulation, checking the overall energy of the configuration at every specified step may be an indicator. When the simulation is reached equilibrium, the overall energy is to reach a steady-state.

In the next section, the generation parameters are analyzed in terms of their effects on amorphous configurations. To achieve that, the Monte Carlo simulation is conducted through an open-access molecular dynamics package, LAMMPS [63, 64]. The benefit of this package is that it offers an efficient and faster calculation of pair potential interactions through predefined potential functions.

5.3 Assessment of Final Configuration

In order to assess the quality and correlation levels of the final configuration, there are some statistical analyses. First of them is known as pair correlation function or radial distribution function, g(R). This is the indicator of scatterer distributions along the configuration. Specifically, it indicates the number of scatterers within distance of (R, R+dR) from a predefined point (or scatterer) as a histogram. The periodicity of scatterers presents itself in g(R) as high peaks at specified distances. When disorder is induced or periodicity is lost, the peaks start to smear out and tend to reach at a steady state value at longer distances. For amorphous photonic materials, observed initial peaks around a couple of unit distances are indicative to short range order, while the g(R) value reaches equilibrium without persisting a peak around the value of 1, for long distances. This shows that the distribution of scatterers at long range is uniform and there is no order.

Second indicator is the spatial Fourier transform of the final configuration. The trans-

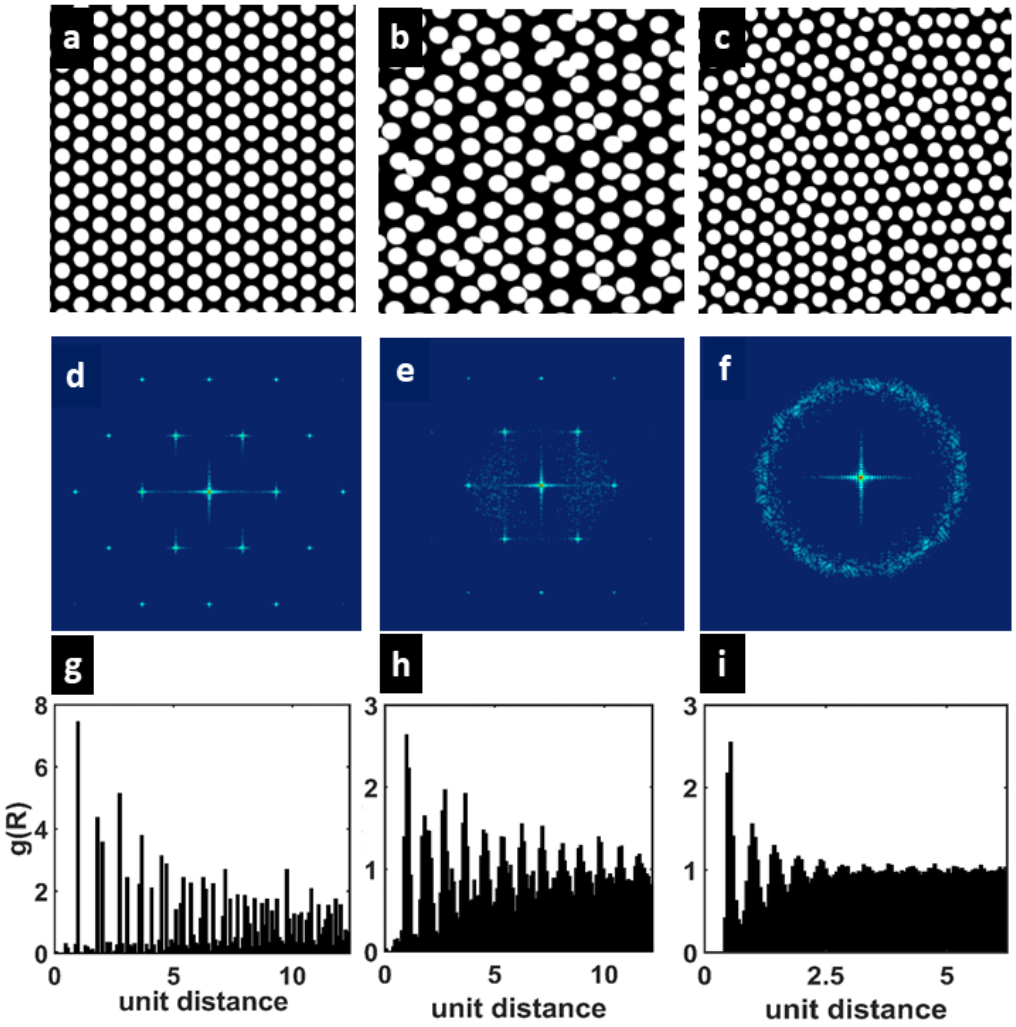

Figure 5.2: Examples of periodic, disordered and amorphous lattice configurations are given. a, Refractive index distribution (n(x,y)) of a photonic crystal with hexagonal lattice. Black regions represent the silicon (Si) slab and white ones are the air holes etched in the slab. b, n(x,y) for the lattice when randomized perturbation is added to each hole position. c, n(x,y) for an amorphous structure where the holes are distributed as a snapshot of atoms in a liquid by the use of the Metropolis Monte Carlo method [11,27] d-f, Fourier transforms of the structures shown in a-c. While the long-range order in the disordered lattice leads to Bragg peaks in the Fourier transform similar to the purely periodic case, there are no peaks shown in the amorphous case. g-i, Radial distribution functions g(R) for the structures a, b, and c. Presence of the peaks over long unit distances is a proof of long-range order. The peaks that are disappearing after a couple of unit distances as provided in i indicate that there is only short-range order.

form is very indicative to recurring patterns along the 2-D plane. Thus, when a periodic lattice is given as input, the periodic pattern which lies inside will present itself in Fourier transform as an array of peaks, which is known as Bragg peaks [18]. The array is identical to the reciprocal lattice of the crystal, which is the basis of photonic band theory. Even a disorder induced photonic crystal lattice shows the underlying long-range order on its Fourier transform. So, for a complete amorphous configuration, the Bragg peaks must not exist. When the equilibrium configuration is verified for lack of long-range order, lack of Bragg peaks is indicative.

There are various parameters that affecting the final configuration. For a simulation utilizing Yukawa potential, these parameters are normalized temperature T^*, screening length l, cutoff radius and number of steps for equilibration. The normalized temperature value is the main factor that determines the degree of randomness along the structure. It is presented before that the acceptance probabilities of moves are depending on Boltzmann factor, which is directly proportional to k_BT. The form of the Boltzmann factor when Yukawa potential is inserted to Metropolis criterion is given at (5.10). The constant in the exponential is used to normalize temperature in the following form of $1/T^* = \frac{\nu_0}{k_BT}$.

$$N(r) \propto exp(\frac{\nu_0}{k_BT} * \frac{e^{-r/l}}{r}) \tag{5.10}$$

In Figure 5.3, it can be seen that while at very high T^*, short range order is lost due to the lack of g(R) peaks, which means the transport of light is halted; at very low T^*, the long range order still persists and one cannot talk about an amorphous structure. In this case, light propagation is still dependent on photonic band structure, which is heavily disturbed by introduced defect modes. For desired transport characteristics, the normalized temperature levels should be at an intermediate level that enables short range order while disperses the long-range periodicity.

Second impacting factor affecting randomness of configuration is screening length l. Screening length is the determining factor that the effective extent of Yukawa potential. In the Figure 5.4, it is shown that the screening length decides how far the order should exist between particles. For lower values, the interaction between two particles become very limited while with increasing screening length, the reach of the

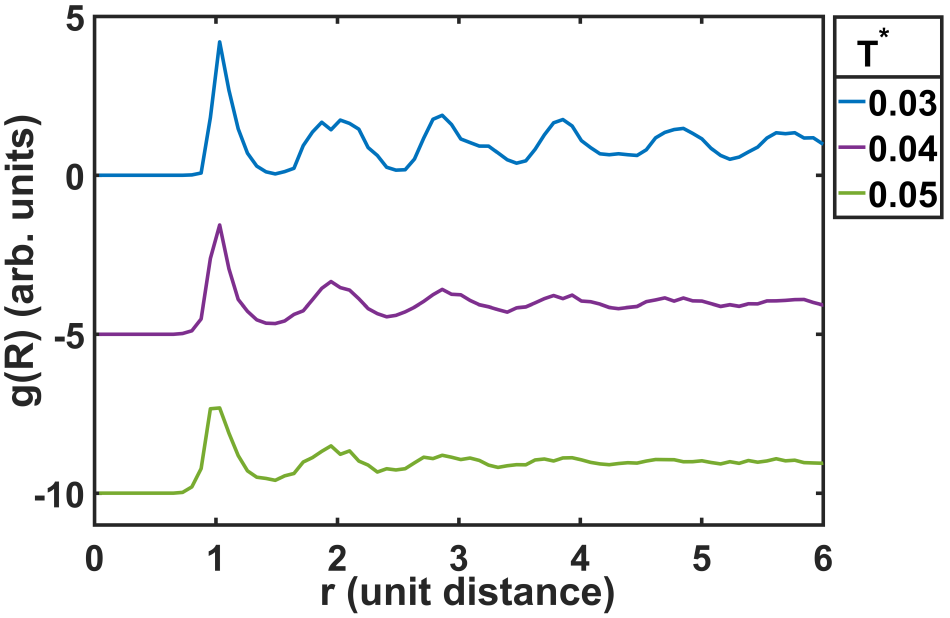

Figure 5.3: At lower bound, disappearance of long range order is shown with gradual increase in normalized temperature parameter, T^*.

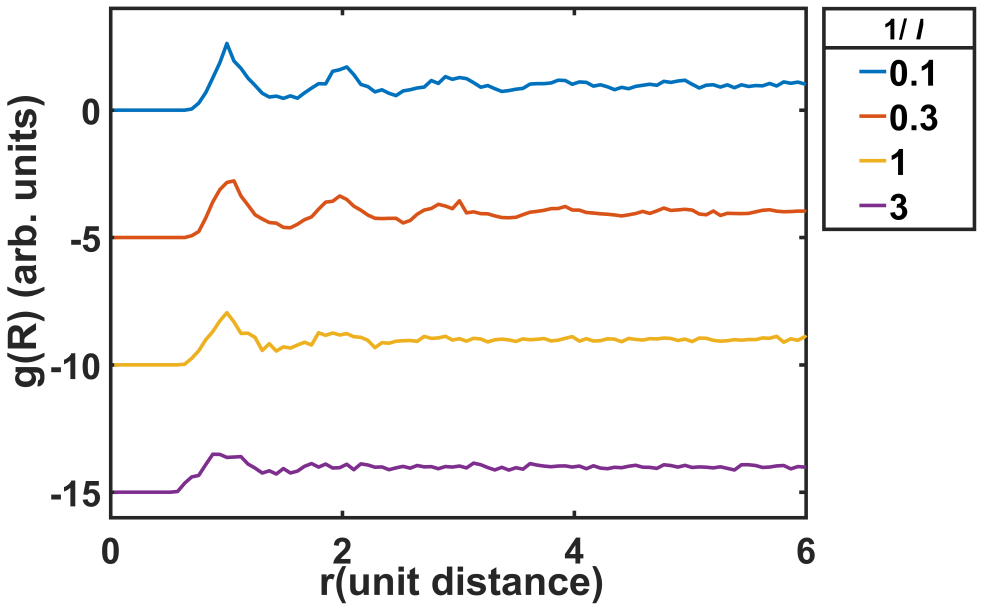

Figure 5.4: Effect of screening length parameter on g(R) is provided. Screening length heavily influences the pair potential between individual scatterers.

potential extends. For an homogeneous configuration, it is the best to use a length comparable to average distance between scatterers of the configuration.

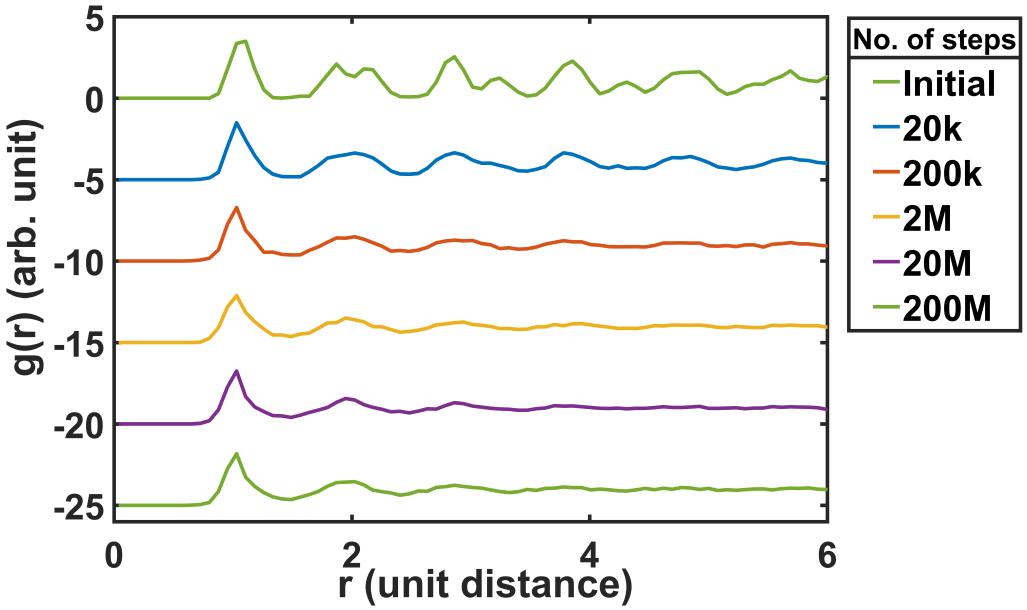

Figure 5.5: The disappearance of long range order with increasing number of steps is analyzed. A step size over two million is shown to be enough to get an amorphous configuration.

The last factor is the number of equilibrating steps. Equilibration time is a combination of various factors such as temperature, acceptance rate and screening length. An indicator for equilibrium can also be obtained through examining evolution of total potential energy of configuration. When the overall energy reaches a plateau, it can be inferred that equilibrium is reached. In this study, it has been observed that the step size over two million is enough to reach equilibrium. The detailed comparison is given in Figure 5.5.

CHAPTER 6

DESIGN AND NUMERICAL ANALYSIS OF AMORPHOUS PHOTONIC MATERIALS

6.1 Design Approach

In order to design an amorphous photonic lattice, a periodic lattice of photonic crystal is an important reference. It is shown before that, the first band gap of an amorphous material and photonic crystal is shared since the first band gap is originated from the short range order of the structure [14]. To preserve short range order, the basic parameters of amorphous material is kept nearly same as photonic crystal. These parameters include lattice constant – a (i.e. average distance between holes in amorphous configuration), and the thickness h and radius r of scatterers. By changing the ratio of radius and thickness versus lattice constant, r/a and h/a, it is possible to play with band gap properties. Here, by scaling the lattice constant, i.e. average spacing of scatterers, the band gap can be shifted to various wavelength regimes. The anticipated change can be easily calculated from obtained band diagram of the corresponding photonic crystal structure. The structure that is modeled is a slab with refractive index of $\sqrt{12}$ which has hexagonal lattice of drilled air holes with refractive index 1 on it. The slab is suspended on air to create an 'air-bridge' structure, which makes the slab waveguide symmetric. So, 1550 nm is targeted as the band gap center and simulated proposed parameters by using the plane-wave eigensolver MPB [33]. The results are analyzed for both TE and TM polarizations and given in Figure 6.1. It is found that, there is a wide band gap around 1550 nm for TE polarization, for the parameters of $r/a = 0.25, h/a = 0.55$, while a equals to 400 nm.The blue region indicates the light cone that the modes are no longer supported inside the slab. The frequency values are normalized with respect to c and a, so that $\lambda = a/f$.

The wavevector indices are along the first Brillouin zone boundaries of the hexagonal lattice.

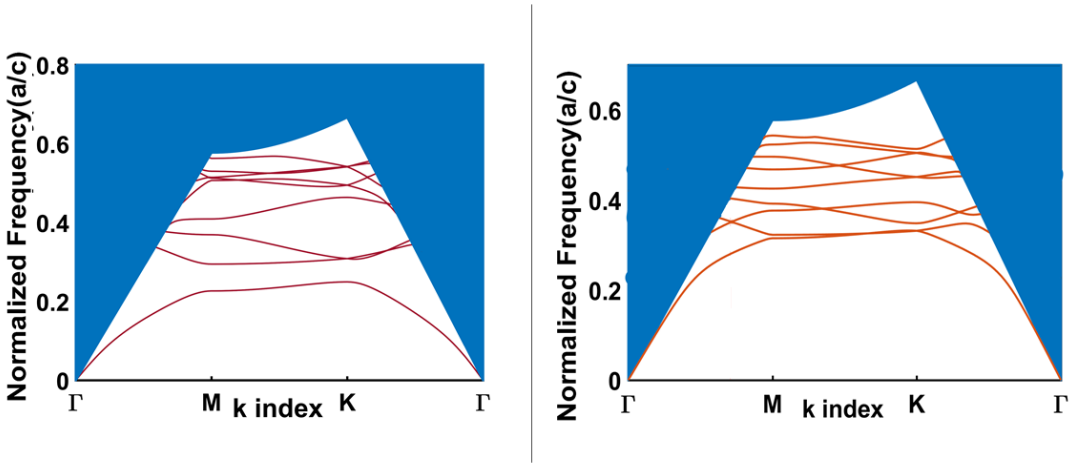

Figure 6.1: Left: TE and Right: TM band diagram of the proposed photonic crystal with $r = 0.10\mu m$, $h = 0.22\mu m$ and $a = 0.4\mu m$ where there is a TE band gap at around 1550 nm.

To verify the band diagram, the transmission spectrum is also computed via FDTD solver, MEEP [32]. The results are normalized with transmission data of a Si slab without any scatterers, to get the transfer function. The simulations are conducted at two different lattice directions $\Gamma - M$ and $\Gamma - K$, since as it can be seen from Figure 6.1, there is a directional dependence on the band gap of the photonic crystal. The overlapping gap wavelengths constitute the real band gap of the structure. Figure 6.2 shows that variation between two direction. It can be seen that the results of transmission analysis is largely fit to the band gap shown by Figure 6.1. The overlapping gap is stretching from $1.37\mu m$ to $1.6\mu m$. Theoretically, the transmission in the gap should be zero for a crystal lattice of infinite extent because there is not any allowed states for propagation. This is not the case for this FDTD simulation, since the simulated domain is finite whose boundaries are defined by PMLs. Thus, it is logical to expect some states to arise due to boundaries, surface etc.

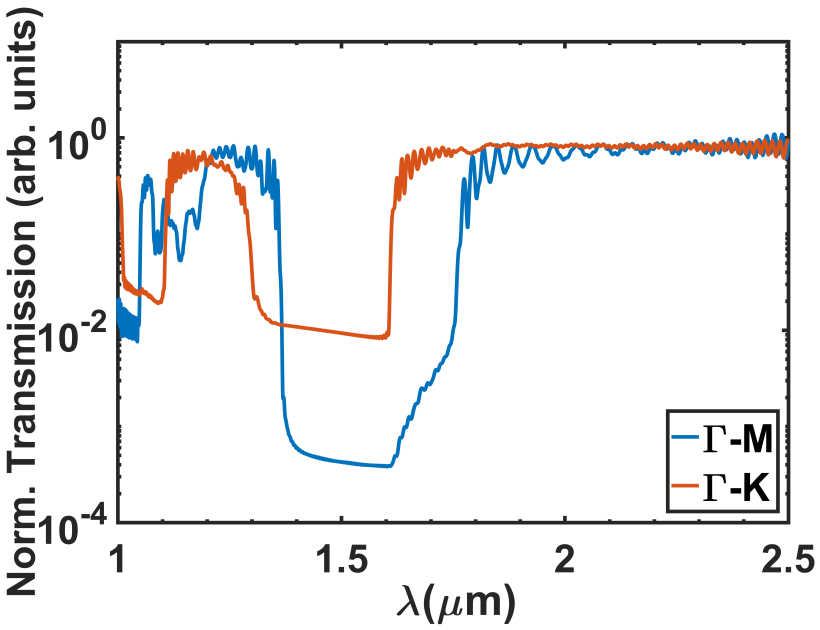

Figure 6.2: TE transmission spectra of the proposed photonic crystal with $r = 0.10\mu m$, $h = 0.22\mu m$ and $a = 0.4\mu m$ for $\Gamma - M$ and $\Gamma - K$ directions.

6.2 Numerical Analysis

Based on this reference, an amorphous photonic material configuration having same dimensions of $h = 0.22\mu m$ and $r = 0.10\mu m$ is implemented. The lattice constant is not exactly applicable for amorphous materials, so to match that, the scatterer coordinates are scaled to have an average pair distance of $0.4\mu m$. The amorphous configurations are generated by Metropolis algorithm that explained before. Yukawa potential is used to model the pair interactions. The screening length is taken as $2.8\mu m$ and at different randomness values to see the effect on band gap. The transmission spectra of the generated configuration is given at Figure 6.3. The band gap approximately spans between $1.36\mu m$ and $1.58\mu m$. It can be seen that, different from photonic crystals, the light propagation is similar for both directions of the lattice, which proves isotropy. Another difference is the presence of dielectric and air band tails entering into the band gap. These tails are comprised of localized states that light can be present but cannot propagate.

Furthermore, the effect of design parameters on the band gap is analyzed. The first parameter is the scatterer size, which is identified by hole radius in this design. The

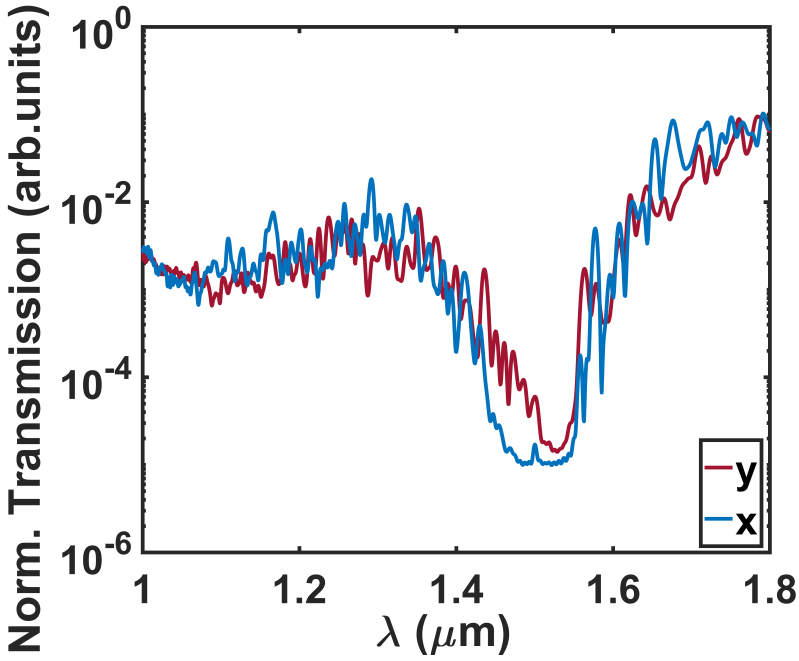

Figure 6.3: The isotropy of the band gap is demonstrated at a specified configuration of $T^* = 0.4$, $r = 0.10\mu m$, $h = 0.22\mu m$ and $a = 0.4\mu m$.

hole radius is mainly affecting the fill-factor of the scatterers inside the material, so also highly related to average refractive index of the whole medium, since the percentage of air regions will change. Since the modes of air band is confined to air regions, a change at air band is expected [2]. Figure 6.4 provides that the band gap shifts to higher frequencies and enlarges with the increase in radius. Moreover, a decrease in the slopes of both band tails is observed. This trend is given at Figure 6.6. In the Figure 6.6, the dotted line shows the wavelength of the least transmission, while the errorbars around indicates the extent between two mobility edges.

Regarding the effect of normalized temperature which defines the randomness among the scatterers, there is not a clear trend as it is given in Figure 6.5 and 6.6. For with increasing disorder up to moderate levels, the preservation of bandgap is observed, with introduction of band tails. In these cases, at least when $T^* < 0.5$, amorphous photonic materials are very suitable to be used in place of photonic crystal band gaps. At higher randomness levels, the short range order becomes damaged, so it is seen that the band gap disappears while transmission halts. Increasing disorder will introduce more localized modes into bandgap, while decreasing overall transmission at other

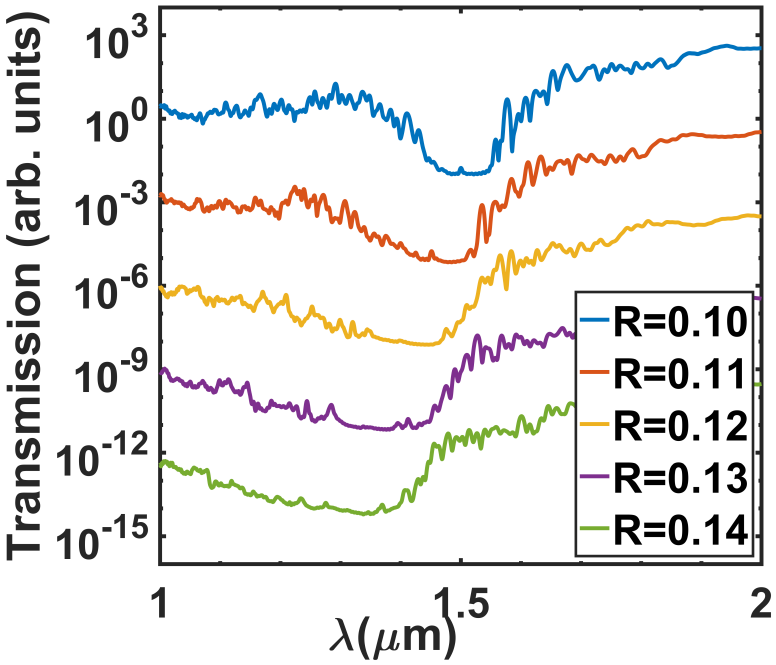

Figure 6.4: The variation of the band gap with hole radius at a specified configuration of $T^* = 0.4$, $h = 0.22\mu m$ and $a = 0.4\mu m$.

parts of spectrum due to increased rate of scattering and decrease in mean free paths.

Furthermore, to understand the field properties of the amorphous material, a cavity and a waveguide structure is simulated and given in Figure 6.7. The cavity simulated is a L1 cavity with one hole missing [2], while the waveguide is prepared by lining a straight array of holes around the line defect in material. This approach is shown as increasing mode confinement and propagation [15].

6.3 Source of Band Tail Asymmetry

In previous sections, the band tail mechanics for the electronic band structure of amorphous semiconductors are explained. Since, Anderson localization is a phenomenon due to general wave mechanics, the analogy between Schrödinger's equation for electrons and the classical wave equation governing light behavior could be exploited. In the case of electronic band tails, the electron states located on bonds between atoms

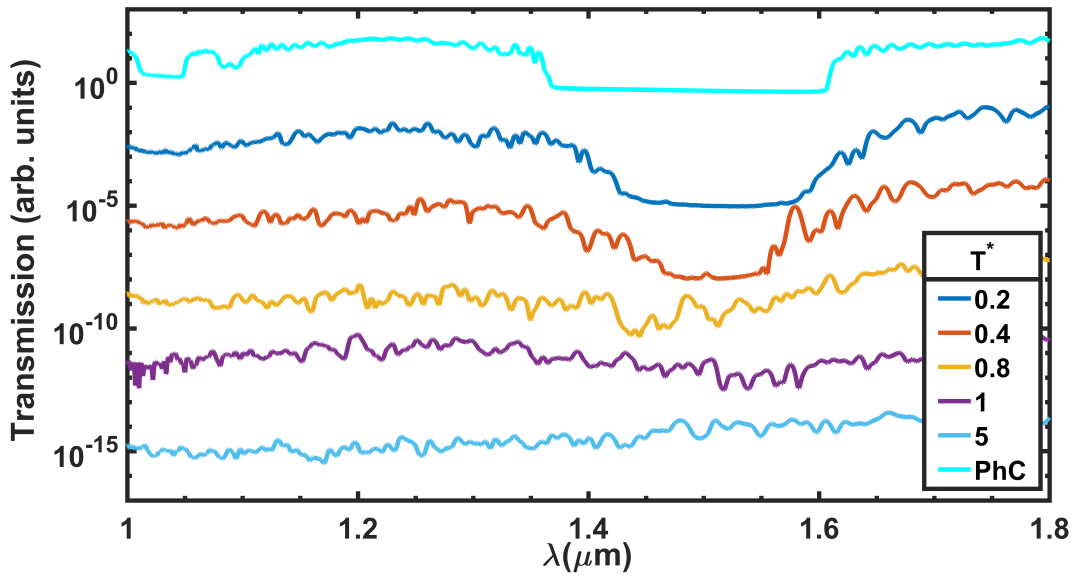

Figure 6.5: The variation of band gap with the normalized temperature - i.e. degree of randomness, for a structure $h = 0.22\mu m$, $r = 0.10\mu m$ and $a = 0.4\mu m$

are modeled according to tight-binding approximation. It is proven that the valence tail states is lying on shorter bonds between atoms, while the conduction band tail states is extending via interactions between atoms with longer distance. Thus, it is explained that the valence tail states is affected more due to local potential variations at short distances [42]. Using same methodology with the help of the abovementioned analogy. In fact, the tight-binding formulation for photonic crystals is done before, by modelling individual scatterers like atoms having overlapping wave functions working with Mie scattering mechanism [65, 66, 17]. It is indicated before that, the properties that affect Urbach parameter are structural, thermal and compositional disorder [37]. Since the amorphous lattices are artificial and static configurations, the slope of the band tail is only depending on the structural disorder. The band tails of a TE gap for an amorphous slab with air holes are observed. As shown in Figure 6.4, the air band tail is smoother with lower slope, while the dielectric band tail preserve its steepness and affected less by randomness. For a TE mode, magnetic field in the air band is confined to the air holes. Since the holes are isolated due to our configuration, it can be postulated that the overlap between mode fields are lower, only between the decaying tails of the field. On the other hand, the dielectric band states

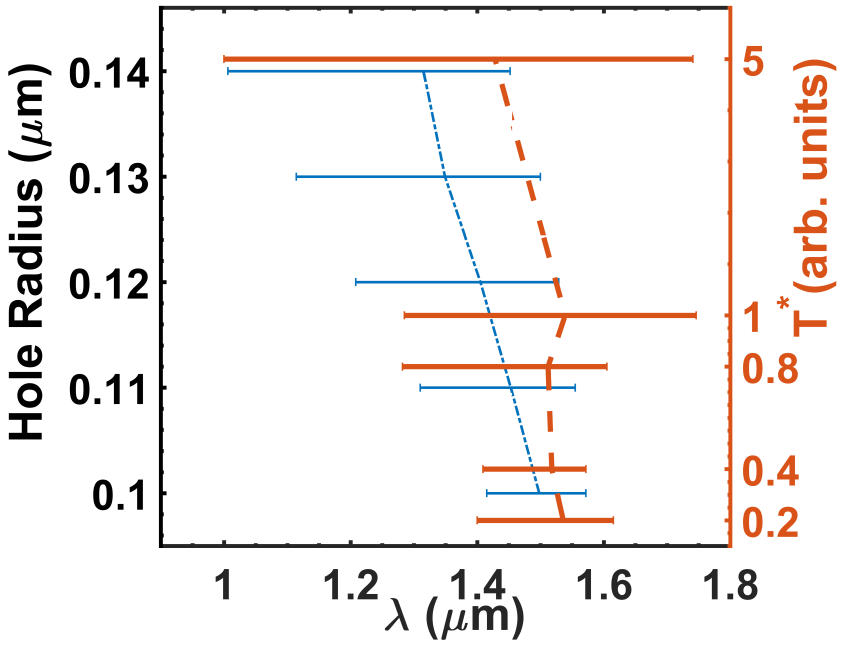

Figure 6.6: The trendlines for variation of band gap with hole radius (blue) and normalized temperature(orange)

in a slab with holes are interconnected through "veins" between the holes. In this case, the wave function is capable of traverse more through the medium and there is a higher overlap between modes. This explanation according to tight-binding model for the amorphous Si, can lead that the air band tail is more susceptible to changes in randomness of the hole configuration as a result. Furthermore, Figure 6.4 reveals that with increasing hole radii, there is a general decrease in the slopes of both dielectric and air band tails. This trend can be attributed to the increase in fill-factor of the holes throughout medium [7]. When the hole radius is increased, the air to dielectric ratio becomes higher; thus the center frequency has begun to increase towards the air band. Simultaneously, the dielectric veins become tighter and reduce the scattering-free length for the traversing fields that make the dielectric band tail more susceptible to the increasing randomness. Another thing to consider is that there is a difference of peak transmission levels between the dielectric mobility edge and air mobility edge. A possible explanation for this may lie in scattering theory [12]. The wavelengths which the dielectric band reside are much longer than the hole feature size; thereby the variations in the refractive index do not affect the fields much, causing high trans-

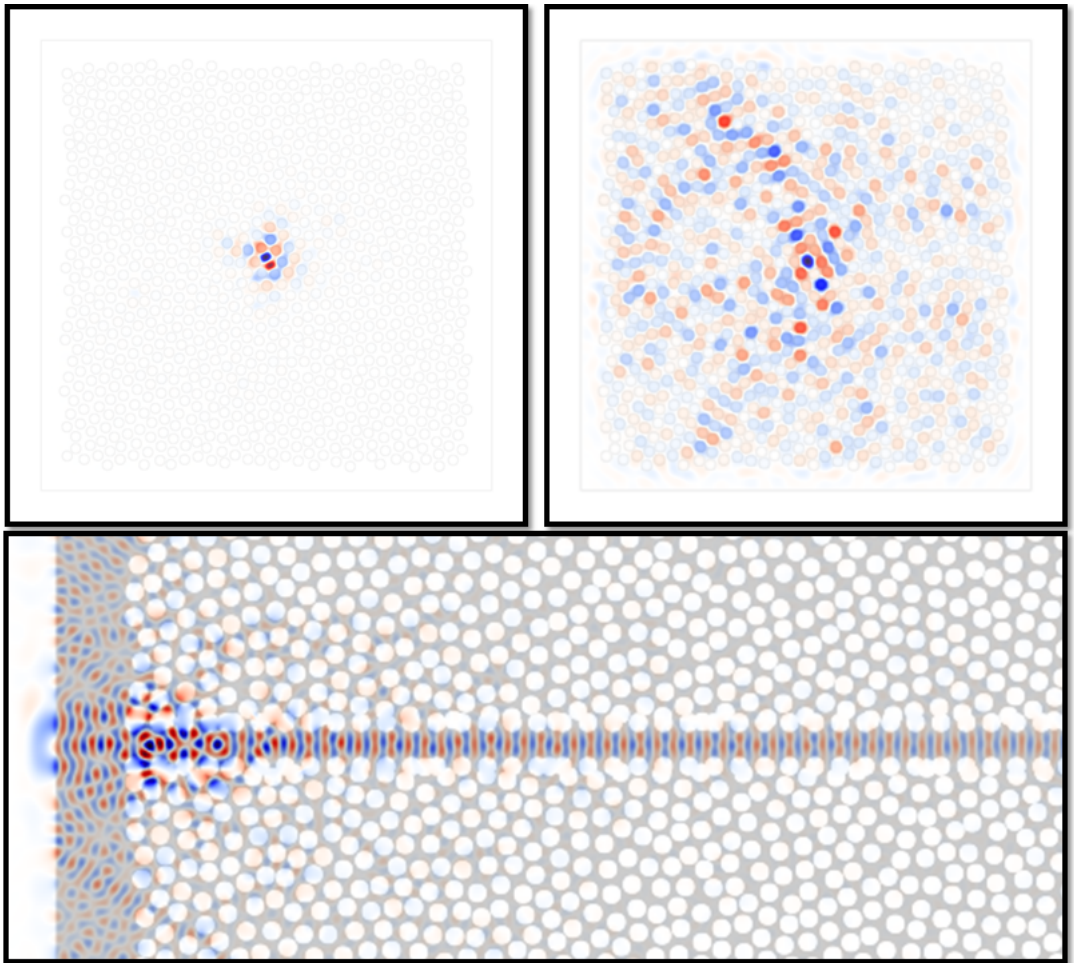

Figure 6.7: A L1 cavity excited with TE mode at Left: bandgap (1550 nm) and Right: band (2000 nm). While mode is remained localized in the band gap of amorphous material, it is largely dissipating outside the band gap, where transmissivity is near unity. Bottom: A waveguide structure is shown to propagate a TE-excited field at bandgap frequency, 1550 nm. To increase confinement, a wall of holes are fabricated alongside direction [15].

mission. This behavior of transmission can also be predicted from Rayleigh scattering behavior [12]. However, the transmission may be disturbed at the wavelengths that are more comparable to the feature size.

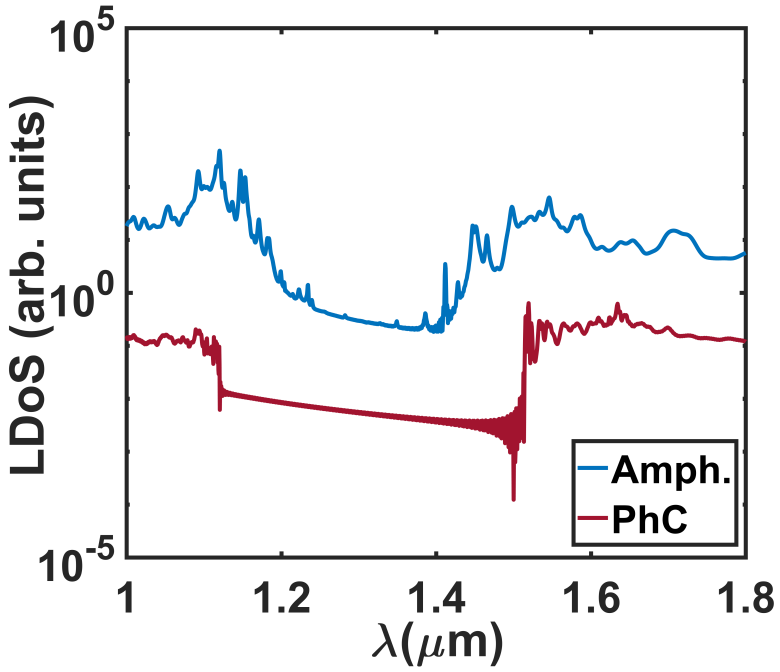

Figure 6.8: The local density of states characteristics for the amorphous slab with air holes at $T^* = 0.4$,$h = 0.22\mu m$, $a = 0.4\mu m$ and $r = 0.10\mu m$ in comparison with the photonic crystal structure with same properties.

In the Figure 6.8, the local density of states characteristics for the $T^* = 0.4$ configuration with $r = 0.13\mu m$ hole radii is provided in comparison with the photonic crystal. With such a comparison, the mobility edges separating band tails are identifiable. Here, the air band tail is stretching from $1.15\mu m$ to $1.35\mu m$ while the dielectric tail states diminish much sharper, between $1.35 - 1.5\mu m$.The relation between density of states and band tails are shown before with a progress from polycrystalline to amorphous distribution of scatterers [17].

To prove the tight-binding analogy, the density of states analysis is repeated for the same amorphous configuration, but reversing the refractive index contrast by using dielectric rods as scatterers instead of air holes . In this case, a TM band gap forms as expected [2]. The electric field of TM mode, which is confined inside the rods,

should have less overlap for dielectric band edge, while the scattering-free length of air band edge modes is larger. Thus, it is expected that the slope of dielectric band tail is smoother than the air band tail due to tight-binding model used for the lattice with air holes. In the Figure 6.9, the local density of states and transmission analyses are

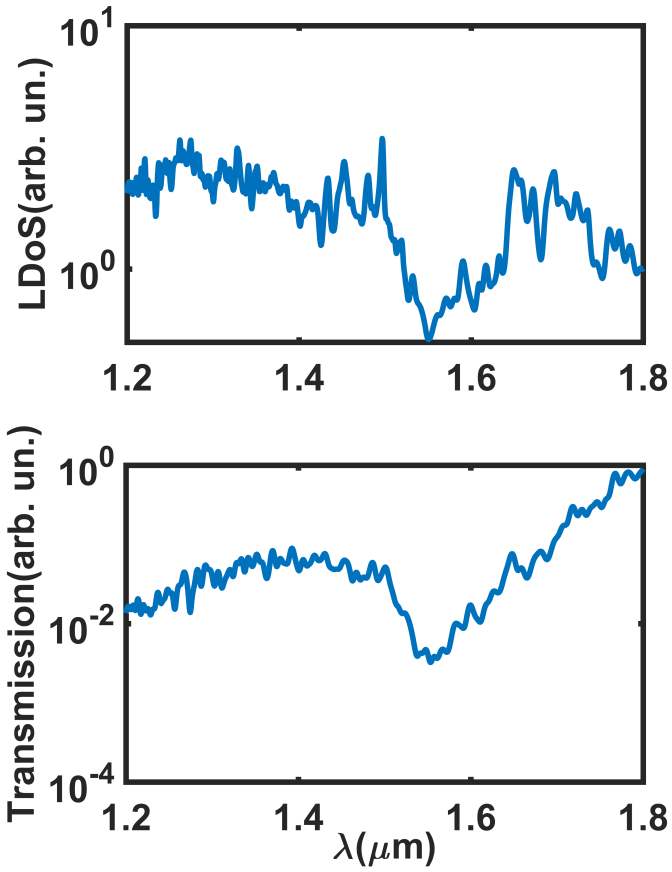

Figure 6.9: LDoS analysis and TM transmission spectrum for a rod configuration with $h = 1.68\mu m$, $r = 0.139\mu m$ and $a = 0.336\mu m$, at the same level of randomness , $T^* = 0.4$.

provided for the rod structure. The band gap regions are stretching from $1.5\mu m$ to $1.65\mu m$ and overlapping in both cases. The air band tail is between 1.5 and $1.55\mu m$ wavelengths, while the dielectric band has a lower slope that decays to the same level as air band tail at only from $1.65\mu m$ to $1.55\mu m$. This proves that the modes confined in the scatterers are more susceptible to randomness, whether they are TE modes in holes or TM modes in rods .

CHAPTER 7

EXPERIMENTAL VERIFICATION

7.1 Fabrication

To verify the existence of band gap in the designed amorphous configurations, test wafers are prepared with different hole radii and randomness. The wafer used is a SOITEC SOI wafer with 220 nm Si layer and 1000 nm Si oxide thickness as insulator. The fabrication is conducted via e-beam lithography. E-beam lithography is particularly useful for prototypes since it does not require a mask. It allows accurate patterning of nanometer features. The mechanism is illuminating an electron-sensitive photoresist material through a focused beam of electrons [67]. The beam width mainly determines the resolution of structure. The photoresist used is polymethyl methacrylate (PMMA), which is a positive resist whose bonds are broken under electron incidence. These broken bonds are cleared through solvent developer, which leaves a positive pattern [68]. This process is followed by inductively coupled plasma (ICP) - reactive ion etching (RIE) to open homogeneous hole structures. The method involves inductively coupling of plasma ions to the substrate via an RF field applied to it. The advantage of this RIE method is that it enables high density plasma while enabling control of ion flux and energy. With this way, it is possible to adjust ion beam for isotropic and anisotropic etching [69]. This patterning is followed by suspension with buffered oxide etchant (BOE) etching to create the "air bridged" structure around the devices shown at Figure 7.1. This membrane-like structure is applied through another photolithograpic step, in which a photoresist mask layer is created. Then, the BOE is infused through the holes of lattice for under-etching for twenty minutes.

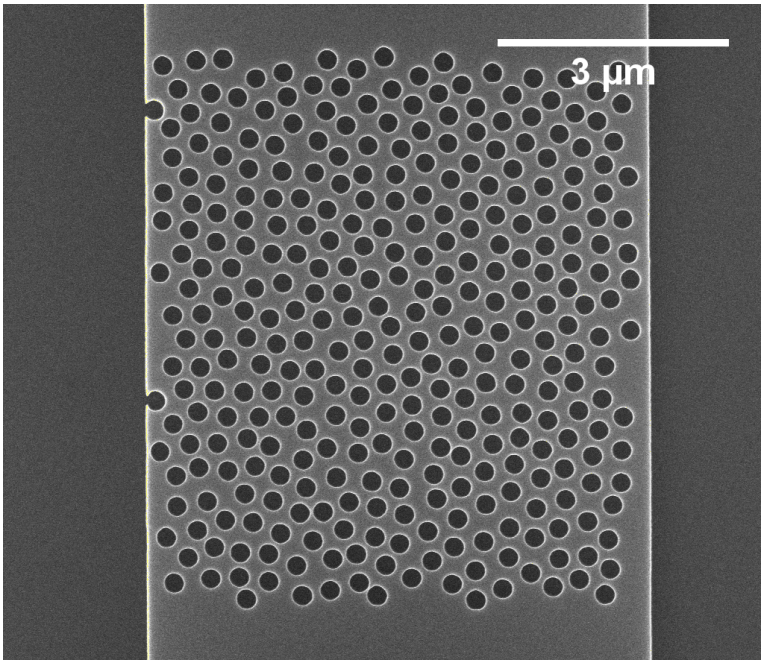

Figure 7.1: An amorphous photonic material configuration with $r = 130nm$ and $t^* = 0.4$.

The configurations are placed into fabricated ridge waveguides that are adiabatically tapered at the port sides and around device, which the taper thickness varies between 450 nm to approximately 6000 nm with a slope of 1 degree angle [70]. The taper is shown at Figure 7.2. Furthermore, for some configurations, there is a S-shaped bent waveguide region is added to separate input and output laterally to avoid interference while measuring which is shown at Figure 7.2.

7.2 Experimental Procedure and Results

To characterize the amorphous configurations, a transmission analysis setup is established. The setup comprises a fiber-output amplified spontaneous emission (ASE) source with a spectrum between 1530-1610 nm wavelengths. The polarization state is linearized with a three-paddle polarization controller and propagated in free-space with the help of a collimator lens. The measured polarization is adjusted by a further free-space polarizer that can be rotated by 360 degrees. To align the laser to the chip, a combination of mirrors and focusing lenses mounted on 3-axis translational stages.

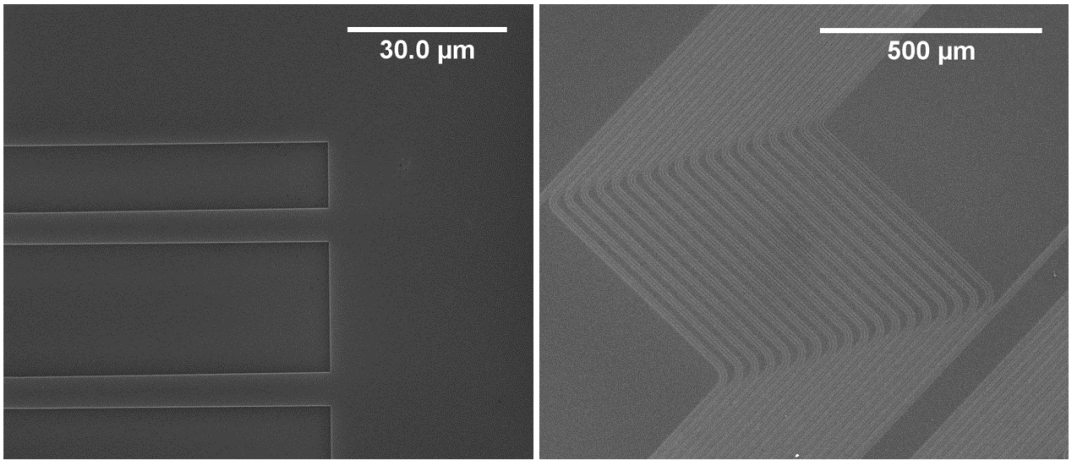

Figure 7.2: Left: Adiabatically designed input taper. The width is decreasing with a very small angle of 1 degrees. Right: The S-shaped bent waveguides added to laterally separate input and output.

The chip is placed on a similar adjustable stage and monitored by a 10x microscope and InGaAs IR focal plane array to observe the position where laser is focused for easier collimation. The output laser is collected by a symmetric path of focusing lens-mirror-collimator lens and fed to the optical spectrum analyzer via fiber. Since the ASE spectrum is non-uniform, experimental data is normalized by ASE spectrum itself which is also measured through one of the waveguides that does not contain any amorphous configuration.

In the Figure 7.4, the experimental data is provided for two different randomness levels and two different hole radii. The measurement is done in the regime of C and L bands, which are the common fiber optical communication bands.The data is fitted to the predicted spectrum and suits well. It can be observed that, there is a 10 dB decrease along dielectric band tail to the midgap as expected from simulations. For a measurement with a supercontinuum bandwidth, all aspects of the spectrum can be resolved.

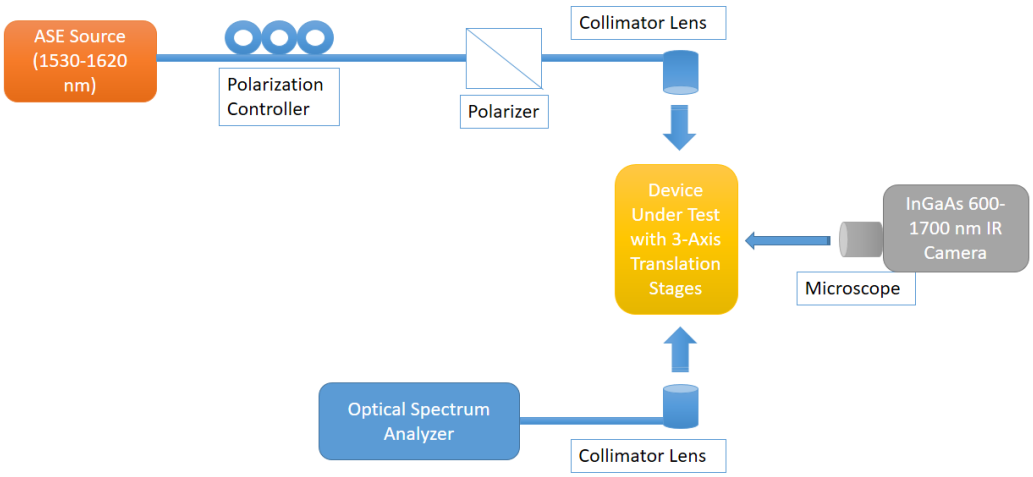

Figure 7.3: The setup diagram for transmission spectral analysis. It is capable of getting measurements at TE and TM polarizations via adjustable polarizer.

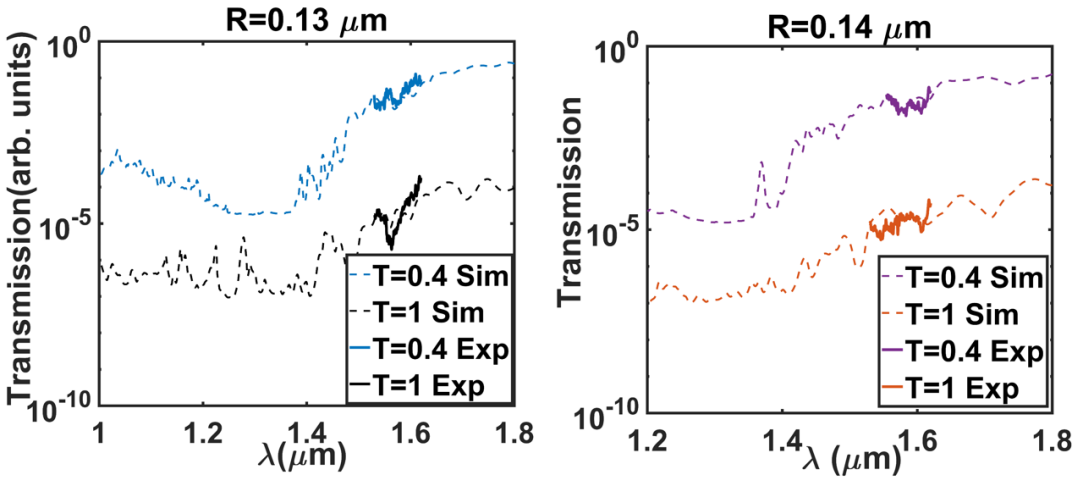

Figure 7.4: The experimental data obtained via an ASE input for the configuration having 130 nm hole radius, at two different randomness levels, 0.4 and 1. The dotted lines in the background are showing the numerical prediction for the actual fabricated structure.

CHAPTER 8

CONCLUSION

In this thesis work, an amorphous photonic material model is proposed and verified experimentally. Amorphous photonic materials are prominent alternatives to photonic crystals by utilizing disorder instead of disturbed by it. In the presence of short-range order, it is shown that photonic band gap still persists and can be used for photonic integrated circuit applications.

In order to design the random refractive index variations, a Metropolis Monte Carlo method based equilibration method is used by considering scatterers as particles in a liquid-like, colloidal medium. The purpose of this approach is to mimic crystalline to amorphous semiconductor conversion. By utilizing Yukawa potential energy function to model particle interactions, the given initial configuration is quenched into a random array of scatterers having only short-range order. The parameters governing the distribution of scatterers; screening length, truncation cutoff and normalized temperature are analyzed, with the increasing number of steps. The generated amorphous configurations are used to form band gaps in air-bridged Si photonic slabs around telecommunication wavelengths of 1550 nm. To determine main parameters of scatterers, a reference photonic crystal is used because of the fact that the first band gap of a photonic material originates from short range order without periodicity requirement. The effect of design parameters on photonic band gap is analyzed to establish a guideline. It is found that for an amorphous slab structure with hole scatterers, increase in the ratio of air to dielectric ratio enlarges the gap bandwidth and shifts the gap center to upper frequencies. Furthermore, the effect of randomness is scrutinized and found that the medium levels of randomness offer the best performance in terms of flexibility and band gap properties. This behavior is demonstrated experimentally

via transmission spectrum measurements for the first time for telecommunications.

The main difference between periodic and random photonic media shows itself in the band tails introduced to band gap. The band tails are a well-studied phenomenon in amorphous semiconductors and related to the electronic density of states. The occurrence of similar states introduced by the localization due to randomness has different characteristics leading to an asymmetry in the bandgap. In this study, the asymmetry of band tails at the band edges are explained with an analogy of tight binding representation of electronic tail states. The reason of asymmetry is regarded to the susceptibility of states to disorder. It is provided that for the slab structure, the air tail states confined in air holes have lesser overlap, which leads to more variation with disorder, while dielectric tail states have more overlap along the slab and less affected by disorder. To prove this postulate, a structure of Si rods as scatterers is used and numerically verified that the case is opposite as expected; that is, the dielectric tail states confined in rods are more susceptible to the disorder.

To sum up, this work presents a guide for amorphous photonic materials to be used for flexible photonic integrated circuit applications. Engineering of amorphous distributions of refractive index and band gaps are analyzed in every aspect. The configurations are verified experimentally and main properties of band gap such as tail asymmetry are theorized through an analogy with electronics of amorphous semiconductors. For future work, the wave propagation in such random media may be explored in depth analytically to understand underlying dynamics further. The demonstration of advanced photonic devices such as ring resonators, filters and modulators can be achieved with the design guidelines presented in this thesis.

REFERENCES

[1] E. Yablonovitch, "Inhibited spontaneous emission in solid-state physics and electronics," *Physical Review Letters*, vol. 58, no. 20, pp. 2059–2062, 1987.

[2] J. J. D. Joannopoulos, S. Johnson, J. N. J. Winn, and R. R. D. Meade, *Photonic Crystals: Molding the Flow of Light*. Princeton University Press, 2008.

[3] K. Edagawa, S. Kanoko, and M. Notomi, "Photonic amorphous diamond structure with a 3D photonic band gap," *Physical Review Letters*, vol. 100, no. 1, pp. 1–4, 2008.

[4] S. Kocaman, M. S. Aras, P. Hsieh, J. F. McMillan, C. G. Biris, N. C. Panoiu, M. B. Yu, D. L. Kwong, A. Stein, and C. W. Wong, "Zero phase delay in negative-refractive-index photonic crystal superlattices," *Nature Photonics*, vol. 5, no. 8, pp. 499–505, 2011.

[5] A. Govdeli, M. C. Sarihan, U. Karaca, and S. Kocaman, "Integrated optical modulator based on transition between photonic bands," *Scientific Reports*, vol. 8, no. 1, p. 1619, dec 2018.

[6] K. C. Kwan, X. Zhang, Z. Q. Zhang, and C. T. Chan, "Effects due to disorder on photonic crystal-based waveguides," *Applied Physics Letters*, vol. 82, no. 25, pp. 4414–4416, 2003.

[7] R. Meisels and F. Kuchar, "Density-of-states and wave propagation in two-dimensional photonic crystals with positional disorder," *Journal of Optics A: Pure and Applied Optics*, vol. 9, no. 9, pp. 396–402, 2007.

[8] V. Savona, "Electromagnetic modes of a disordered photonic crystal," *Physical Review B - Condensed Matter and Materials Physics*, vol. 83, no. 8, pp. 1–15, 2011.

[9] M. M. Sigalas, C. M. Soukoulis, C. T. Chan, R. Biswas, and K. M. Ho, "Effect

of disorder on photonic band gaps," *Physical Review B*, vol. 59, no. 20, pp. 12 767–12 770, 1999.

[10] A. A. Asatryan, P. A. Robinson, L. C. Botten, R. C. McPhedran, N. A. Nicorovici, and C. Martijn De Sterke, "Effects of geometric and refractive index disorder on wave propagation in two-dimensional photonic crystals," *Physical Review E - Statistical Physics, Plasmas, Fluids, and Related Interdisciplinary Topics*, vol. 62, no. 4 B, pp. 5711–5720, 2000.

[11] S. John, "Electromagnetic absorption in a disordered medium near a photon mobility edge," *Physical Review Letters*, vol. 53, no. 22, pp. 2169–2172, 1984.

[12] S. John, "Strong localization of photons in certain disordered dielectric superlattices," *Physical Review Letters*, vol. 58, no. 23, p. 2486, 1987.

[13] C. M. Soukoulis, E. N. Economou, G. S. Grest, and M. H. Cohen, "Existence of anderson localization of classical waves in a random two-component medium," *Physical Review Letters*, vol. 62, no. 5, 1989.

[14] C. Jin, X. Meng, B. Cheng, Z. Li, and D. Zhang, "Photonic gap in amorphous photonic materials," *Physical Review B*, vol. 63, no. 19, p. 195107, apr 2001.

[15] H. Miyazaki, M. Hase, H. T. Miyazaki, Y. Kurokawa, and N. Shinya, "Photonic material for designing arbitrarily shaped waveguides in two dimensions," *Physical Review B*, vol. 67, no. 23, p. 235109, jun 2003.

[16] M. Florescu, S. Torquato, and P. J. Steinhardt, "Designer disordered materials with large, complete photonic band gaps," *Proceedings of the National Academy of Sciences*, vol. 106, no. 49, pp. 20 658–20 663, dec 2009.

[17] J. K. Yang, C. Schreck, H. Noh, S. F. Liew, M. I. Guy, C. S. O'Hern, and H. Cao, "Photonic-band-gap effects in two-dimensional polycrystalline and amorphous structures," *Physical Review A - Atomic, Molecular, and Optical Physics*, vol. 82, no. 5, pp. 1–8, 2010.

[18] M. Rechtsman, A. Szameit, F. Dreisow, M. Heinrich, R. Keil, S. Nolte, and M. Segev, "Amorphous photonic lattices: Band gaps, effective mass, and suppressed transport," *Physical Review Letters*, vol. 106, no. 19, pp. 1–4, 2011.

[19] S. Kocaman, J. F. McMillan, D. Wang, M. C. Rechtsman, and C. W. Wong, "Observation of band gaps in amorphous photonic structures with different temperatures in the near infrared," *Conference on Lasers and Electro-Optics Europe - Technical Digest*, vol. 2014-Janua, pp. 2–3, 2014.

[20] B. E. A. Saleh and M. C. Teich, "Fundamentals of Photonics , 2nd Edition," p. 1200, 2007.

[21] C. G. Bostan, "Design and fabrication of quasi-2d photonic crystal components based on silicon-on-insulator technology," Ph.D. dissertation, University of Twente, 2005.

[22] K. Sakoda, *Optical Properties of Photonic Crystals*, ser. Springer Series in Optical Sciences. Berlin/Heidelberg: Springer-Verlag, 2005, vol. 80.

[23] C. Kittel, *Introduction to Solid State Physics*. John Wiley and Sons, Inc., New York, 2004, vol. 8th edition.

[24] A. Taflove, A. Oskooi, and S. G. Johnson, *Advances in FDTD computational electrodynamics: photonics and nanotechnology*. Artech House, 2013.

[25] E. Purcell, "Spontaneous emission probabilities at radio frequencies," *Phys. Rev.*, vol. 69, p. 681, 1946.

[26] K. Busch and S. John, "Photonic band gap formation in certain self-organizing systems," *Physical Review E*, vol. 58, no. 3, pp. 3896–3908, 1998.

[27] L. Van Hove, "The occurrence of singularities in the elastic frequency distribution of a crystal," *Physical Review*, vol. 89, no. 6, p. 1189, 1953.

[28] K. Yee, "Numerical solution of initial boundary value problems involving maxwell's equations in isotropic media," *IEEE Transactions on Antennas and Propagation*, vol. 14, no. 3, pp. 302–307, 1966.

[29] Y. Hao and R. Mittra, *FDTD Modeling of Metamaterials: Theory and Applications*. Artech House, 2008.

[30] J.-P. Berenger, "A perfectly matched layer for the absorption of electromagnetic waves," *Journal of Computational Physics*, vol. 114, no. 2, pp. 185–200, oct 1994.

[31] L. Chrostowski and M. Hochberg, *Silicon Photonics Design: from Devices to Systems*. Cambridge University Press, 2015.

[32] A. F. Oskooi, D. Roundy, M. Ibanescu, P. Bermel, J. Joannopoulos, and S. G. Johnson, "Meep: A flexible free-software package for electromagnetic simulations by the FDTD method," *Computer Physics Communications*, vol. 181, no. 3, pp. 687–702, 2010.

[33] S. Johnson and J. Joannopoulos, "Block-iterative frequency-domain methods for Maxwell's equations in a planewave basis," *Optics Express*, vol. 8, no. 3, p. 173, 2001.

[34] C. R. Pollock and M. Lipson, *Integrated Photonics*. Springer, 2003, vol. 20, no. 25.

[35] C. F. Klingshirn, *Semiconductor Optics*. Springer Science & Business Media, 2012.

[36] R. Zallen, *The Physics of Amorphous Solids*. Weinheim, Germany: Wiley-VCH Verlag GmbH, 1998.

[37] I. Studenyak, M. Kranj, and M. Kurik, "Urbach rule in solid state physics," *International Journal of Optics and Applications*, vol. 4, no. 3, pp. 76–83, 2014.

[38] F. Urbach, "The long-wavelength edge of photographic sensitivity and of the electronic absorption of solids," *Physical Review*, vol. 92, no. 5, pp. 1324–1324, dec 1953.

[39] D. A. Drabold and J. Dong, "Band tail states and the Anderson transition in amorphous silicon," *Journal of Non-Crystalline Solids*, vol. 227-230, no. May, pp. 153–157, 1998.

[40] P. W. Anderson, "Absence of diffusion in certain random lattices," *Physical Review*, vol. 109, no. 5, pp. 1492–1505, 1958.

[41] B. R. Djordjević, M. F. Thorpe, and F. Wooten, "Computer model of tetrahedral amorphous diamond," *Physical Review B*, vol. 52, no. 8, pp. 5685–5689, 1995.

[42] D. A. Drabold, Y. Li, B. Cai, and M. Zhang, "Urbach tails of amorphous silicon," *Physical Review B - Condensed Matter and Materials Physics*, vol. 83, no. 4, pp. 1–6, 2011.

[43] P. A. Fedders, D. A. Drabold, and S. Nakhmanson, "Theoretical study on the nature of band-tail states in amorphous Si," *Physical Review B*, vol. 58, no. 23, pp. 15 624–15 631, 1998.

[44] S. Aljishi, J. D. Cohen, S. Jin, and L. Ley, "Band tails in hydrogenated amorphous silicon and silicon-germanium alloys," *Physical Review Letters*, vol. 64, no. 23, pp. 2811–2814, 1990.

[45] P. Sheng, *Introduction to Wave Scattering, Localization and Mesoscopic Phenomena*. Springer Science & Business Media, 2006, vol. 88.

[46] L. Tsang and A. Ishimaru, "Backscattering enhancement of random discrete scatterers," *JOSA A*, vol. 1, no. 8, pp. 836–839, 1984.

[47] M. P. Van Albada and A. Lagendijk, "Observation of weak localization of light in a random medium," *Physical Review Letters*, vol. 55, no. 24, p. 2692, 1985.

[48] P.-E. Wolf and G. Maret, "Weak localization and coherent backscattering of photons in disordered media," *Physical Review Letters*, vol. 55, no. 24, p. 2696, 1985.

[49] D. S. Wiersma, P. Bartolini, A. Lagendijk, and R. Righini, "Localization of light in a disordered medium," *Nature*, vol. 390, no. 6661, pp. 671–673, 1997.

[50] E. Abrahams, P. Anderson, D. Licciardello, and T. Ramakrishnan, "Scaling theory of localization: Absence of quantum diffusion in two dimensions," *Physical Review Letters*, vol. 42, no. 10, p. 673, 1979.

[51] N. F. Mott, "Electrons in disordered structures," *Advances in Physics*, vol. 16, no. 61, pp. 49–144, 1967.

[52] H. De Raedt, A. Lagendijk, and P. De Vries, "Transverse localization of light," *Physical Review Letters*, vol. 62, no. 1, pp. 47–50, 1989.

[53] T. Schwartz, G. Bartal, S. Fishman, and M. Segev, "Transport and Anderson localization in disordered two-dimensional photonic lattices," *Nature*, vol. 446, no. 7131, pp. 52–55, 2007.

[54] P. Hsieh, C. Chung, J. F. McMillan, M. Tsai, M. Lu, N. C. Panoiu, and C. W. Wong, "Photon transport enhanced by transverse Anderson localization in disordered superlattices," *Nature Physics*, vol. 11, no. 3, pp. 268–274, 2015.

[55] M. Shell. (2012) Monte Carlo methods. Accessed on April 28, 2018. [Online]. Available: https://engineering.ucsb.edu/~shell/che210d/Monte_Carlo.pdf

[56] D. Frenkel and B. Smit, *Understanding Molecular Simulation: From Algorithms to Applications*. Academic Press, 2001, vol. 1.

[57] N. Metropolis and S. Ulam, "The monte carlo method," *Journal of the American Statistical Association*, vol. 44, no. 247, pp. 335–341, 1949.

[58] N. Metropolis, A. W. Rosenbluth, M. N. Rosenbluth, A. H. Teller, and E. Teller, "Equation of state calculations by fast computing machines," *The Journal of Chemical Physics*, vol. 21, no. 6, pp. 1087–1092, 1953.

[59] S. Erkoç, "Empirical many-body potential energy functions used in computer simulations of condensed matter properties," *Physics Reports*, vol. 278, no. 2, pp. 79–105, 1997.

[60] H. Yukawa, "On the interaction of elementary particles," *Proceedings of the Physico-Mathematical Society of Japan. 3rd Series*, vol. 17, pp. 48–57, 1935.

[61] I. Suwan, H. Hussein, A. Hussein, and M. Daragmeh, "The optimum cut-off radius in Monte Carlo simulation of Yukawa potential point particles," *Journal of Physics: Conference Series*, vol. 869, no. 1, p. 012054, 2017.

[62] A.-P. Hynninen and M. Dijkstra, "Phase diagrams of hard-core repulsive Yukawa particles," *Physical Review E*, vol. 68, no. 2, p. 021407, 2003.

[63] S. Plimpton, "Fast parallel algorithms for short-range molecular dynamics," *Journal of Computational Physics*, vol. 117, no. 1, pp. 1–19, 1995.

[64] LAMMPS Molecular Dynamics Simulator. Accessed on May 28, 2018. [Online]. Available: http://lammps.sandia.gov

[65] K. Edagawa, "Photonic crystals, amorphous materials, and quasicrystals," *Science and Technology of Advanced Materials*, vol. 15, no. 3, p. 034805, 2014.

[66] E. Lidorikis, M. Sigalas, E. Economou, and C. Soukoulis, "Tight-Binding Parametrization for Photonic Band Gap Materials," *Physical Review Letters*, vol. 81, no. 7, pp. 1405–1408, 1998.

[67] M. Altissimo, "E-beam lithography for micro-nanofabrication," *Biomicrofluidics*, vol. 4, no. 2, p. 026503, 2010.

[68] P. Rai-Choudhury, *Handbook of Microlithography, Micromachining, and Microfabrication*. IET, 1997, vol. 1.

[69] H.-a. Mehedi, V. Mille, J. Achard, O. Brinza, and A. Gicquel, "Effect of the process parameters of inductively coupled plasma reactive ion etching on the fabrication of diamond nanotips," *Physica Status Solidi (A)*, vol. 211, no. 10, pp. 2343–2346, 2014.

[70] S. G. Johnson, P. Bienstman, M. A. Skorobogatiy, M. Ibanescu, E. Lidorikis, and J. D. Joannopoulos, "Adiabatic theorem and continuous coupled-mode theory for efficient taper transitions in photonic crystals," *Phys. Rev. E*, vol. 66, p. 066608, 2002.